







Impact of mid-Z gas fill on dynamics and performance of shock-driven implosions at the OMEGA laser

M. Gatu Johnson ^{1,*}, P. J. Adrian ¹, B. D. Appelbe ², A. J. Crilly,² C. J. Forrest,³ V. Yu. Glebov ³, L. M. Green ⁴, B. M. Haines,⁴ N. V. Kabadi,¹ G. Kagan,² B. D. Keenan,⁴ J. Kunimune,¹ C. K. Li,¹ O. M. Mannion,⁵ R. D. Petrasso,¹ F. H. Séguin,¹ H. W. Sio,⁶ C. Stoeckl,³ G. D. Sutcliffe ¹, W. T. Taitano,⁴ and J. A. Frenje¹

¹*Massachusetts Institute of Technology Plasma Science and Fusion Center, Cambridge, Massachusetts 02139, USA*

²*Centre for Inertial Fusion Studies, The Blackett Laboratory, Imperial College, London SW7 2AZ, United Kingdom*

³*Laboratory for Laser Energetics, University of Rochester, Rochester, New York 14623, USA*

⁴*Los Alamos National Laboratory, Los Alamos, New Mexico 87545, USA*

⁵*Sandia National Laboratories, Albuquerque, New Mexico 87185, USA*

⁶*Lawrence Livermore National Laboratory, Livermore, California 94550, USA*



(Received 20 January 2021; accepted 24 April 2024; published 3 June 2024)

Shock-driven implosions with 100% deuterium (D_2) gas fill compared to implosions with 50:50 nitrogen-deuterium (N_2D_2) gas fill have been performed at the OMEGA laser facility to test the impact of the added mid-Z fill gas on implosion performance. Ion temperature (T_{ion}) as inferred from the width of measured DD-neutron spectra is seen to be $34\% \pm 6\%$ higher for the N_2D_2 implosions than for the D_2 -only case, while the DD-neutron yield from the D_2 -only implosion is 7.2 ± 0.5 times higher than from the N_2D_2 gas fill. The T_{ion} enhancement for N_2D_2 is observed in spite of the higher Z, which might be expected to lead to higher radiative loss, and higher shock strength for the D_2 -only versus N_2D_2 implosions due to lower mass, and is understood in terms of increased shock heating of N compared to D, heat transfer from N to D prior to burn, and limited amount of ion-electron-equilibration-mediated additional radiative loss due to the added higher-Z material. This picture is supported by interspecies equilibration timescales for these implosions, constrained by experimental observables. The one-dimensional (1D) kinetic Vlasov-Fokker-Planck code iFP and the radiation hydrodynamic simulation codes HYADES (1D) and xRAGE [1D, two-dimensional (2D)] are brought to bear to understand the observed yield ratio. Comparing measurements and simulations, the yield loss in the N_2D_2 implosions relative to the pure D_2 -fill implosion is determined to result from the reduced amount of D_2 in the fill (fourfold effect on yield) combined with a lower fraction of the D_2 fuel being hot enough to burn in the N_2D_2 case. The experimental yield and T_{ion} ratio observations are relatively well matched by the kinetic simulations, which suggest interspecies diffusion is responsible for the lower fraction of hot D_2 in the N_2D_2 relative to the D_2 -only case. The simulated absolute yields are higher than measured; a comparison of 1D versus 2D xRAGE simulations suggest that this can be explained by dimensional effects. The hydrodynamic simulations suggest that radiative losses primarily impact the implosion edges, with ion-electron equilibration times being too long in the implosion cores. The observations of increased T_{ion} and limited additional yield loss (on top of the fourfold expected from the difference in D content) for the N_2D_2 versus D_2 -only fill suggest it is feasible to develop the platform for studying CNO-cycle-relevant nuclear reactions in a plasma environment.

DOI: [10.1103/PhysRevE.109.065201](https://doi.org/10.1103/PhysRevE.109.065201)

I. INTRODUCTION

The inertial confinement fusion (ICF) platform has been previously established [1,2] as an important complement to traditional accelerator experiments for studying nucleosynthesis-relevant nuclear reactions, as the reactions occur in a plasma environment that more closely mimics the interior of a star [1]. This platform has already been successfully used to study several reactions relevant to nucleosynthesis, including ${}^3\text{He} + {}^3\text{He}$ [3], $\text{T} + {}^3\text{He}$ [3,4], $\text{T} + \text{T}$ [5–7], and $p + \text{D}$ [8]. The goal of the experiments described in this paper was to test the feasibility of extending this platform to

allow exploration of mid-Z reactions, which would only be possible if sufficiently high ion temperature (T_{ion}) and yields could be achieved with mid-Z implosion gas fill. Initial feasibility studies applying fuel composition and reactivity scaling from pure D_2 -gas-filled implosions suggest this would be feasible as long as the added mid-Z gas does not substantially degrade the implosions in terms of T_{ion} or yield. Shock-driven implosions of thin CH shells filled with 100% deuterium (D_2) gas or 50:50 nitrogen-deuterium (N_2D_2) gas, with total fill pressure and number density conserved between the two implosion types, were undertaken at the OMEGA laser facility [9] to test this. The results presented here show $34\% \pm 6\%$ higher T_{ion} as inferred from the broadening of measured DD-neutron spectra and a 7.2 ± 0.5 times lower DD-neutron yield for the N_2D_2 than for the pure D_2 -fill implosions.

*gatu@psfc.mit.edu

The observed changes in T_{ion} and yield represent quantitative signatures of how the added mid-Z gas fill impacts implosion dynamics, which is the subject of this paper. A number of different physics effects are expected to impact the dynamics of these shock-driven implosions with low initial fill gas density and long ion-ion mean free paths, including differential shock heating of the different ion species, interspecies equilibration and diffusion, three-dimensional asymmetries, radial and directional flows, electron viscosity, and radiative loss. Comparison of simulation and measurements allows conclusions to be drawn about the importance of different physics effects in these implosions. No single simulation tool is currently expected to capture all of these effects. Different aspects of the problem are considered through comparison of data with output from one-dimensional (1D) and two-dimensional (2D) xRAGE radiation hydrodynamics simulations [10–12], from the Vlasov-Fokker-Planck (VFP) code iFP [13–18], and from 1D HYADES [19]. In summary,

(i) xRAGE is used to address impact of asymmetries and electron viscosity, and as a state-of-the-art hydrodynamic benchmark.

(ii) iFP is used to address the multi-ion dynamics of differential shock heating, interspecies equilibration, and diffusion.

(iii) The simple HYADES code was used to design the experiments, and is included for reference as well as to provide initial conditions for iFP.

The simulations are described in Sec. IV. The implosions are expected to be highly kinetic in nature, with long ion-ion mean free paths relative to system scale size; this suggests that a kinetic treatment such as that done by iFP can be expected to better capture the implosion dynamics.

The enhanced T_{ion} is concluded to arise from enhanced shock heating of N and subsequent heat transfer from N to D in combination with heat loss from the implosion core prior to burn that is insufficient for completely counteracting the extra heating efficiency. This conclusion is supported by burn-averaged ion-ion and electron-ion equilibration rates calculated from the observables. A fourfold DD-neutron yield difference is expected because of the lower D content in the N_2D_2 compared to the D_2 -only implosions. Simulations suggest the remaining (1.8-fold) difference arises because of a smaller fraction of the D_2 getting hot enough to burn in the N_2D_2 case. Unlike previous yield anomaly observations [20–22], the measured yield ratio is relatively closely reproduced in both kinetic and hydrodynamic simulations, with hydrodynamic simulations suggesting radiative cooling at the implosion edges and kinetic simulations enhanced diffusion of D versus N as the responsible mechanism.

While the implosions studied here are entirely shock driven, the results are also instructive in terms of fully understanding integrated inertial confinement fusion experiments, where a series of shocks sets the stage for the subsequent compression. The novel mid-Z gas fill provides an extreme test of the capabilities of the codes in terms of ability to handle multi-ion effects that might be important also for integrated DT or surrogate D^3He experiments; if the codes can capture the N-D dynamics, the expectation is that they should be able to capture the less extreme (in terms of mass/charge difference between the ion species) DT or D^3He scenarios. Previous experimental [23], theoretical [24,25], and kinetic

modeling [26–30] studies have suggested that multi-ion and kinetic effects may be important in this context.

While the present experiments represent the first use of N as a majority fill gas, the results can be contrasted to earlier experiments with trace amounts of higher-Z gas in the fill. Gases such as Ar or Kr are routinely used in implosions as a spectroscopic tracer. Such experiments have previously shown evidence of diffusion-driven stratification between the Ar tracer and D_2 fuel [31–33]. Early experiments with varying amounts of Ar, Kr, and Xe dopant also showed enhanced DD-neutron yield reduction and increased x-ray emission with increased dopant concentration [34–36]. In addition, Ar has been recently tested as a fill gas in mix experiments using deuterated macrofoams, where nuclear observables from foam-filled capsules with HT and ArT gas fill were compared [37]. The macrofoam experiments are significantly more compressive than the present shock-driven experiments, and because of the foam structure they also contain a large amount of carbon. However, the ArT-filled experiments also show reduced shock yield compared to the HT-filled experiments, qualitatively consistent with the reduced yield seen for the N_2D_2 compared to D_2 -only implosions in the present case. Deuterated macrofoam experiments with Au dopant also show substantial impact of the high-Z dopant on yield and x-ray emission [38].

The paper is organized as follows. Section II summarizes the experimental setup, while Sec. III presents the results and discusses the implications of the experimental observables in terms of underlying physics, including equilibration times and mean free paths. Section IV introduces the hydrodynamic and kinetic simulation tools used to model the experiments, including a discussion about their capabilities and limitations; as discussed above, none are expected to fully capture the physics of these implosions, but between them they help shed light on shock heating dynamics, interspecies equilibration and diffusion, asymmetries, impact of radial and directional flows, and radiative loss. In Sec. V, the simulations are brought to bear to understand the observed yield ratio between implosions with N_2D_2 versus D_2 -only fill. In Sec. VI, the effects of shell diffusion and electron viscosity on these implosions are considered. Section VI also includes a discussion about impacts of flows on measured T_{ion} , which are found not to explain the observed T_{ion} differences between the two fill types. Section VII concludes the paper.

II. EXPERIMENTAL SETUP

The experimental setup parameters are summarized in Table I and Fig. 1. The laser was delivered in a 1-ns square pulse. Due to constraints imposed by other experiments on the same shot day, 51 of the 60 available OMEGA laser beams were used, phase plates were not installed, and no beam smoothing was used; the beam spot size was enlarged by setting the lens position to 1.8 mm. The nine missing beams form a single cone, leading to a directional drive deficit in the direction (100° , 270°) polar, azimuthal angle. The laser intensity profile on capsule was simulated using the VISRAD code [39], with the resulting profile illustrated in Fig. 1(b). Also indicated in this image are the directions of the weak spot

TABLE I. Implosion characteristics and performance parameters for the thin CH shell D_2 and N_2D_2 gas-filled implosions. T_{ion} is found to be 1.34 ± 0.06 times higher for the N_2D_2 -gas-filled than for the D_2 -only gas-filled implosions, while the yield is found to be 7.2 ± 0.5 times higher for the D_2 -only gas-filled than for the N_2D_2 -gas-filled implosions.

Shot	Fill type	E_{laser} (kJ)	Absorb. laser (%)	Capsule parameters				DD- n performance parameters			
				OD (μm)	CH shell thickness (μm)	$n_{ion,init}$ (10^{20} cm^{-3})	ρ_{init} (mg/cm^3)	n yield ($\times 10^9$)	T_{ion} (keV)	Bang time (ps)	Burn width (ps)
92978	N_2D_2	24.5	65	870	6.9	2.2	2.8	2.9 ± 0.2	13.16 ± 0.54	870 ± 112	n/a
92979	D_2	25.2	64	869	6.8	2.1	0.7	21.0 ± 1.1	10.07 ± 0.34	745 ± 54	130
92980	N_2D_2	25.2	67	876	6.7	2.2	2.8	3.0 ± 0.3	13.75 ± 0.56	780 ± 112	n/a

and capsule stalk mount, which visibly impact the implosion as can be seen in the measured x-ray image in Fig. 1(c). The impact of this asymmetry on implosion performance is

assessed by comparing 1D and 2D xRAGE simulations (see Sec. IV). Importantly, the asymmetry is the same for N_2D_2 and D_2 -only gas-filled implosions, allowing for direct comparison of experimental observables from the two implosion types.

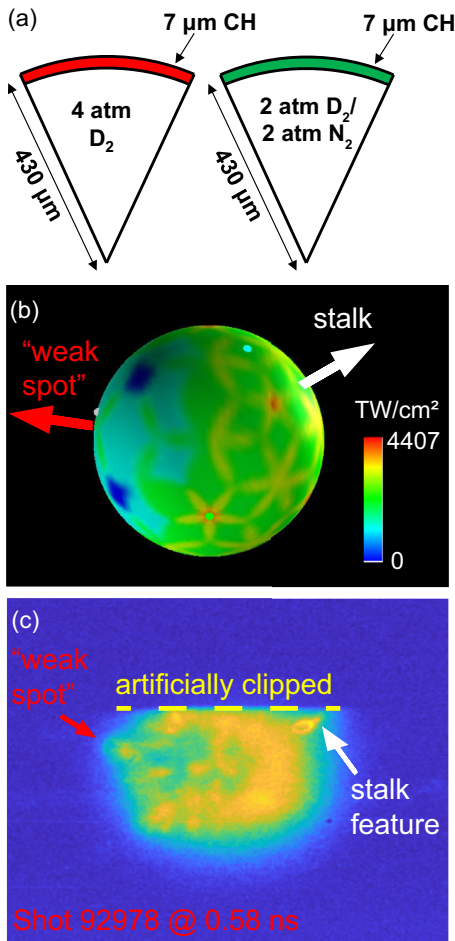


FIG. 1. (a) Cartoons of D_2 and N_2D_2 gas-filled capsules used in these experiments, and (b) a VisRad-calculated map of the laser intensity on capsule, illustrating the weak spot (red arrow) at polar and azimuthal angles $\theta = 100^\circ$ and $\varphi = 270^\circ$ arising from the 51-beam laser drive. The location of the stalk mount holding the capsule in the chamber is shown by the white arrow. This image displays the capsule from $\theta, \varphi = 142.6^\circ, 342^\circ$, which is also the viewing angle for the self-emission framing camera imager used to obtain the image shown in (c). Features in the image correlate with the capsule stalk mount and the drive weak spot. (Note that the image is clipped at the top due to diagnostic misalignment.)

III. EXPERIMENTAL RESULTS AND UNDERSTANDING THE T_{ion} OBSERVATIONS

This section describes the key experimental results. The observables are used to calculate characteristic parameters, and implications of the results in terms of implosion dynamics are discussed. In particular, burn-averaged interspecies equilibration times calculated from observables are shown to support the conjecture that the higher observed DD-neutron-spectrum-inferred T_{ion} from the N_2D_2 than from the D_2 implosions is due to enhanced shock heating of N versus D and subsequent heat transfer from N to D, in combination with limited heat transfer from ions to electrons, and hence susceptibility to radiative heat loss. The experimental observables alone do not explain the amount of DD- n yield reduction observed between the D_2 and N_2D_2 implosions; this effect is examined further with the support of simulations in Sec. V.

The measured neutron yields, T_{ion} , bang times, and burn width are shown in Table I. Yields and T_{ion} are measured with neutron time-of-flight (nTOF) detectors [40,41]. T_{ion} is inferred from the broadening of measured DD-neutron spectra [42], which means it also captures any broadening due to non-thermal flows [43–48]; however, the widths are dominated by thermal broadening in these experiments as discussed in more detail in Sec. VI. Bang times and burn widths are measured with the neutron temporal diagnostic (NTD) [49]. The systematic bang-time uncertainty for NTD is estimated to be ± 50 ps. The sensitivity of NTD is such that at 3×10^9 yield, only ~ 10 neutrons interact with the scintillator. This is not enough to infer a burn width, and also leads to substantial uncertainty in the inferred bang time as seen in Table I. At 2.1×10^{10} yield, ~ 70 neutrons are expected to interact, leading to a statistical burn width uncertainty of $\sim 12\%$; the total uncertainty remains to be fully quantified, which is why no error bar is quoted for the burn width. Note that the measured burn width reported in Table I has been corrected for a 20-ps FWHM scintillator transit time, 40-ps FWHM response width, and $(778 \times d \times \sqrt{T_{ion}})$ -ps FWHM (with distance $d = 0.03$ m and T_{ion} in keV) thermal spectrum broadening [49]. (Note that the OMEGA nTOF suite includes a large number of detectors capable of handling yields ranging from $\sim 10^7$ to 10^{14} . In contrast to the NTD, signal quality is good at 3×10^9 yield.

Statistical uncertainty is also considered in the reported error bars.)

Time-integrated and time-resolved x-ray imaging data were also obtained from these implosions. Based on these results, which are discussed in detail in Appendix A, a DD burn radius of $100 \pm 40 \mu\text{m}$ is estimated for both the N_2D_2 and pure D_2 -fill implosions. (Note that the x-ray emission cannot be expected to correspond directly to the region of nuclear burn from these implosions; this is also discussed in Appendix A.)

As can be seen in Table I, T_{ion} is found to be 1.34 ± 0.06 times higher for the N_2D_2 gas-filled than for the D_2 -only gas-filled implosions. A few notes must be made about the interpretation of this result:

(i) Viscous ion heating within a plasma shock is expected to scale linearly with individual ion mass as $T_{\text{ion}} \sim m_{\text{ion}} v_{\text{shock}}^2$ [50]. Ion shock heating scaling with mass is also supported by recent experimental work [51,52]. This means shock heating of N can be expected to be seven times more efficient than the heating of D at the same shock strength. As the primary observable in this experiment is the DD- n emission, from which apparent T_{ion} is inferred [42], enhanced heating of N must be transferred to D before it can be observed.

(ii) Adding N_2 in the fuel means substantially increasing the electron density, n_e , which consequently increases the radiative loss rate through bremsstrahlung emission; this can be naively expected to cool and “dud” the implosion.

(iii) Since the total mass of the N_2D_2 fuel is higher and hence its shock strength weaker [22] (HYADES simulations give a shock Mach number of 3.8 for the N_2D_2 and 4.9 for the D_2 implosions), the shock is expected to heat the D less in the N_2D_2 implosions than in the D_2 -only implosions (same individual ion mass, different shock velocity).

(iv) T_{ion} as inferred from the DD- n neutron spectrum will be impacted by any plasma flows at burn. However, such effects cannot explain the observed T_{ion} difference between the N_2D_2 and D_2 -only fill, as discussed in detail in Sec. VI.

(v) In principle, since yield depends on ion density and temperature, the higher average T_{ion} inferred from the N_2D_2 than from the D_2 implosions could also result if the radial ion temperature profiles were the same in the two cases, but the neutron emission was more heavily weighted to the high-temperature regions in the N_2D_2 implosions due to more centrally peaked radial density profiles. All simulations brought to bear on these experiments suggest that this is not the case (see Figs. 3 and 4 and surrounding discussion).

With this context, it is concluded that the D in the N_2D_2 implosions must get its additional heat compared to the D_2 -only case from N through N-D ion-ion equilibration (τ_{ND}). In addition, the T_{ion} data suggest that the impact of the radiative loss on the timescale of burn in the N_2D_2 implosions is limited. Given that the bremsstrahlung must be higher in the N_2D_2 than in the D_2 -only case, the most likely explanation for this is that the electron-ion equilibration time (τ_{ei}) is slow enough that the electron heat loss does not propagate to the ions prior to burn. These conjectures are examined further in the next section.

Yield is found to be 7.2 ± 0.5 times higher for the D_2 -only gas-filled than for the N_2D_2 -gas-filled implosions. The added N_2 replaces half of the D_2 , which means the initial D number

TABLE II. Burn-averaged equilibration times for the N_2D_2 implosions. The equilibration-rate calculations require information on T_{ion} , electron temperature T_e , and ion and electron number densities n_i and n_e . The number densities are estimated by scaling the initial number density (calculated from the initial fill pressure) based on the initial and final radii of the implosions as $n_{\text{final}} = n_{\text{init}} \times r_{\text{init}}^3 / r_{\text{final}}^3$, with r_{final} for these implosions constrained by measurements to $100 \pm 40 \mu\text{m}$ (see Appendix A). T_e in these implosions was not measured, but similar implosions have shown $T_e \sim 4.5 \text{ keV}$ [53]. This number is consistent with simulated T_e (see Figs. 4 and 13). The apparent T_{ion} inferred from the broadening of measured DD-neutron spectra is used as baseline, which can be inflated by $\sim 1 \text{ keV}$ due to flows as discussed in Sec. VI, prompting a lower limit of $T_{\text{meas}} - 1 \text{ keV}$ to be used for T_{D} . For T_{N} , values ranging from measured T_{ion} to $T_{\text{N}} = 2T_{\text{D}}$ are used in the calculations. This range was determined based on simulations (see Secs. V and VI).

$r_{\text{final}} (\mu\text{m})$	Assumptions			Equilibration times (ps)				
	$T_{\text{D}} (\text{keV})$	$T_{\text{N}} (\text{keV})$	$T_e (\text{keV})$	τ_{DD}	τ_{NN}	τ_{eD}	τ_{ND}	τ_{eN}
100	13.5	13.5	4.5	444	0.5	390	20	55
100	12.5	24.9	4.5	399	1.2	390	21	55

density n_d in the N_2D_2 implosion is 0.5 times that in the D_2 -only implosions. As the DD- n yield scales as n_d^2 , a factor of 4 in yield reduction is expected from the change in fuel composition, with a factor of 1.8 remaining to be explained by additional physics. Note in this context that because the N_2D_2 and D_2 -only fills are not hydrodynamically equivalent, the implosion dynamics are not expected to be identical. This could lead to different final density profiles, which would then mean local variations in the factor-of-4 yield reduction estimate; however, globally, this is the expected effect of difference in D content alone. The implications of the yield ratio result are discussed further with the aid of simulations in Sec. V.

A. Equilibration rates and their implications

The observed enhancement in T_{ion} inferred from the DD-neutron spectrum in the N_2D_2 versus D_2 -only gas-filled implosions points to the following:

(i) N is heated more than D and transfers some of its additional heat to D on the timescale of the implosion.

(ii) τ_{ei} is too long to allow enhanced radiative loss from the N_2D_2 compared to D_2 -only gas-fill implosions to excessively cool the ions prior to burn. (Radiative loss will only be observable in the nuclear emission if τ_{ei} is short enough to allow propagation of the cooling to the ion population on the timescale of burn.)

These two conjectures are supported by burn-averaged interspecies equilibration rates calculated from observables. The interspecies equilibration times for the N_2D_2 implosions are calculated in Table II for the considered implosion conditions. The first thing to note is that the D-D equilibration time τ_{DD} is long enough that D-D equilibration is virtually negligible on the timescale of the implosion. This is a manifestation of the kinetic nature of the D ions in these implosions. The second thing to note is that $\tau_{\text{eD}} \gg \tau_{\text{eN}}$, and that the impact of e-D equilibration is virtually negligible. The third thing to note is that the τ_{NN} is short enough where the N population

TABLE III. Knudsen numbers N_k calculated for deuterium and nitrogen. Note that these calculations assume $T_{\text{ion}} = T_{\text{D}} = T_{\text{N}} = T_{\text{DDn, meas}}$ and a length scale $R = r_{\text{final}} = 100 \mu\text{m}$.

Shot	Fill	N_k (deuterium)	N_k (nitrogen)
92978	N_2D_2	0.7	0.004
92979	D_2	1.6	n/a
92980	N_2D_2	0.7	0.004

is expected to be immediately internally equilibrated, and hence to be well captured by a hydrodynamic model. This leaves τ_{ND} and $\tau_{e\text{N}}$ as the primary factors of interest in these implosions. With a measured burn width of $\tau_{\text{burn}} \approx 130$ ps (corrected for instrumental broadening), these two equilibration times are not negligible. As shown in Table II, $\tau_{\text{ND}} \ll \tau_{e\text{N}}$, suggesting that N transfers heat to D much faster than it loses heat to the electrons, consistent with the T_{ion} -based conjectures. This result also continues to hold over a wide range of assumptions (for example, although $\tau_{e\text{N}}$ is nearly independent on T_{N} because of its weighting with m_e while τ_{ND} scales with $T_{\text{N}}^{3/2}$, T_{N} would have to be very high before $\tau_{\text{ND}} > \tau_{e\text{N}}$). (Note that the interspecies equilibration times are calculated considering equilibration in both directions, $i - j$ and $j - i$, and assuming full ionization. While the burn-averaged equilibration times are calculated in this section, equilibration times will vary spatially and temporally throughout the dynamically evolving implosions. See Appendix B.)

B. Quantifying the kinetic nature of the implosions

The equilibration-rate calculations above suggest that the N population should be well described by a hydrodynamic treatment, while the deuterium population is more susceptible to long mean-free-path effects such as diffusion. The Knudsen number N_k , defined as $N_k = \lambda_{\text{ii}}/R$, where λ_{ii} is the ion-ion mean free path and R a characteristic length scale for the implosion, has been proposed as a metric for quantifying the importance of such kinetic effects [54,55]. $N_k \ll 1$ means mean free paths are short relative to system scale size with a hydrodynamic description expected to hold, while a kinetic treatment is required to accurately model implosion dynamics otherwise. The observables used in the equilibration-rate calculations above are also used to calculate N_k , with the results summarized in Table III. Here, r_{final} is used as the characteristic length scale R . Given that the mean free path $\lambda_{\text{ii}} = v_{\text{th}}/n_{\text{ii}} \propto T_{\text{ion}}^{1/2}/T_{\text{ion}}^{-3/2} = T_{\text{ion}}^2$, and that $\lambda_{\text{ii}} \propto n_i^{-1}$ or (since $n_i \propto 1/\text{volume}$) $\lambda_{\text{ii}} \propto r_{\text{final}}^3$, leading to $N_k \propto r_{\text{final}}^2$, N_k will increase rapidly with increasing T_{ion} and r_{final} . N_k is calculated separately for D and N; due to the higher Z of N relative to D, N_k for N is virtually negligible, while N_k for D (calculated considering N-D and D-D collisions) is significant for both implosion types. Since our observables come from reactions between D ions, N_k as calculated for D is the relevant parameter to consider. The high values of $N_{k,\text{D}}$ as shown in Table III suggest that a kinetic treatment is required to accurately model these implosions; the iFP code was brought to bear to address this as discussed in Sec. IV. (N_k will also vary spatially and

temporally throughout the dynamically evolving implosions. See Appendix B.)

IV. SIMULATIONS

While the observables alone constrain an overall picture of the dynamics of these implosions as described above, contrasting them to simulation provides a test of both the observation-based conjecture as well as the capabilities of the simulations to capture the physics at play in these unique implosions with majority mid-Z fill. Simulations are also invoked to understand the yield difference observed between the D_2 and N_2D_2 implosions. As stated in the Introduction, no single simulation tool is anticipated to capture all the physics expected to impact the implosion dynamics, which include multi-ion effects such as differential shock heating, interspecies equilibration and diffusion, kinetic effects due to long ion-ion mean free paths, electron viscosity, radiative loss, and three-dimensional effects due to the laser drive asymmetry and capsule stalk mount. Three different simulation tools were brought to bear to elucidate different aspects of the physics. The state-of-the-art radiation hydrodynamics code xRAGE [10–12] is used to address impact of asymmetries, directional flow, and electron viscosity, and also provides hydrodynamic yield and T_{ion} predictions for comparison to observables. The 1D average-ion radiation hydrodynamics code HYADES [19] was used for preshot design simulations, and is included for completeness as well as to provide the initial conditions for kinetic VFP simulations using the code iFP [13–18]. iFP uniquely provides a test of the impact of kinetic effects and also treats N and D as separate species, allowing a window into differential shock heating, interspecies diffusion, and ion-ion equilibration effects. Each of the three codes is briefly described in this section; results from the codes are then used below to address the meaning of the difference in DD- n yield observed between D_2 -only and N_2D_2 implosions (Sec. V), and the impact of shell diffusion, electron viscosity, and flow and non-Maxwellian effects on T_{ion} (Sec. VI). Calculated T_{ion} and yield from each of the simulations are summarized and compared to measurements in Table IV and Fig. 2.

The Eulerian xRAGE radiation hydrodynamic simulation code [10–12], developed by Los Alamos National Laboratory, was run in 1D and 2D mode to explicitly assess the asymmetry effect on yield and T_{ion} , and found a fourfold reduction in yield and 30% reduction in T_{ion} for both implosion types (N_2D_2 and D_2 gas fill) with the 2D asymmetry considered (Table V). Implosion performance is reduced in two versus one dimension because of temporal smearing (differences in timing of shock traverse across θ/φ) of the converging shocks, leading to weaker shocks and less heating. The 2D simulations explicitly model the laser drive weak spot as well as the capsule stalk mount, albeit in directly opposing geometry due to the 2D limitation (in the experiment, the weak spot and stalk mount are separated by 137° ; see Fig. 1). They also include nominal surface roughness for OMEGA implosions (but show that the CH remains out of the burn region since most of the yield occurs at the shock flash; there is no mixing due to hydrodynamic instability). For the remainder of this discussion, only 2D xRAGE results are considered. xRAGE has

TABLE IV. Simulated T_{ion} (obtained from the width of synthetic neutron spectra to allow direct comparison to measurements) and yield for the D_2 -only and N_2D_2 implosions. Measured values (with the average quoted for the repeat N_2D_2 implosions) are also given for comparison.

Gas fill	2D xRAGE		iFP with C+H		HYADES		Measured	
	T_{ion} (keV)	DD- n yield	T_{ion} (keV)	DD- n yield	T_{ion} (keV)	DD- n yield	T_{ion} (keV)	DD- n yield
D_2 only	10.71	1.8×10^{11}	12.59	5.8×10^{10}	20.4	5.9×10^{11}	10.1 ± 0.3	$(2.1 \pm 0.1) \times 10^{10}$
N_2D_2	20.44	2.9×10^{10}	15.71	9.8×10^9	33.6	6.2×10^{10}	13.5 ± 0.4	$(2.9 \pm 0.2) \times 10^9$

some reduced models for kinetic physics, including plasma transport driven by species concentration, electron and ion pressure, and electron and ion temperature gradients as well as plasma viscosity [56]. These models use a diffusion approximation that considers shell diffusion and is valid for small N_k , and were employed for the simulations presented in this paper. xRAGE is also capable of considering two separate ion species, albeit at the same temperature; however, this feature was not used in the simulations of the present implosions. xRAGE features adaptive mesh refinement, SESAME tabular equations of state, laser ray tracing using the Laboratory for Laser Energetics Mazinisin package [57], multigroup radiation diffusion with OPLIB opacities, and flux-limited electronic and ionic thermal heat conduction. The 2D xRAGE simulated T_{ion} and yield ratios are contrasted to data in Fig. 2, with absolute numbers found in Tables I and IV. The xRAGE-simulated T_{ion} for the D_2 -only implosion very closely matches measured values, while T_{ion} for the N_2D_2 implosion overpredicts the measurement by ~ 7 keV. The yield ratio between the N_2D_2

and D_2 -only implosions is relatively well captured, while the absolute yields are about an order of magnitude high; part of this difference is likely due to the three-dimensional (3D) nature of the imposed asymmetry.

Simulations using the relatively simple 1D, Lagrangian, radiation hydrodynamics code HYADES [19] were run primarily to provide initial conditions for the iFP simulations. The HYADES simulations used multigroup radiative energy transport, SESAME tabular equations of state, an average local thermodynamic equilibrium (LTE) ionization model, and an electron flux limiter of 0.065, resulting in yields and T_{ion} that are substantially higher than measured (compare Table I and Table IV). (While the measured bang time does not strongly constrain the simulation energetics due to its large uncertainty, varying the HYADES flux limiter to give results within the bang-time uncertainty bounds shows that the HYADES-simulated yield and T_{ion} are insensitive to these variations to within 13%.) Part of the reason for this is the 1D nature of HYADES, which cannot be expected to capture the asymmetries

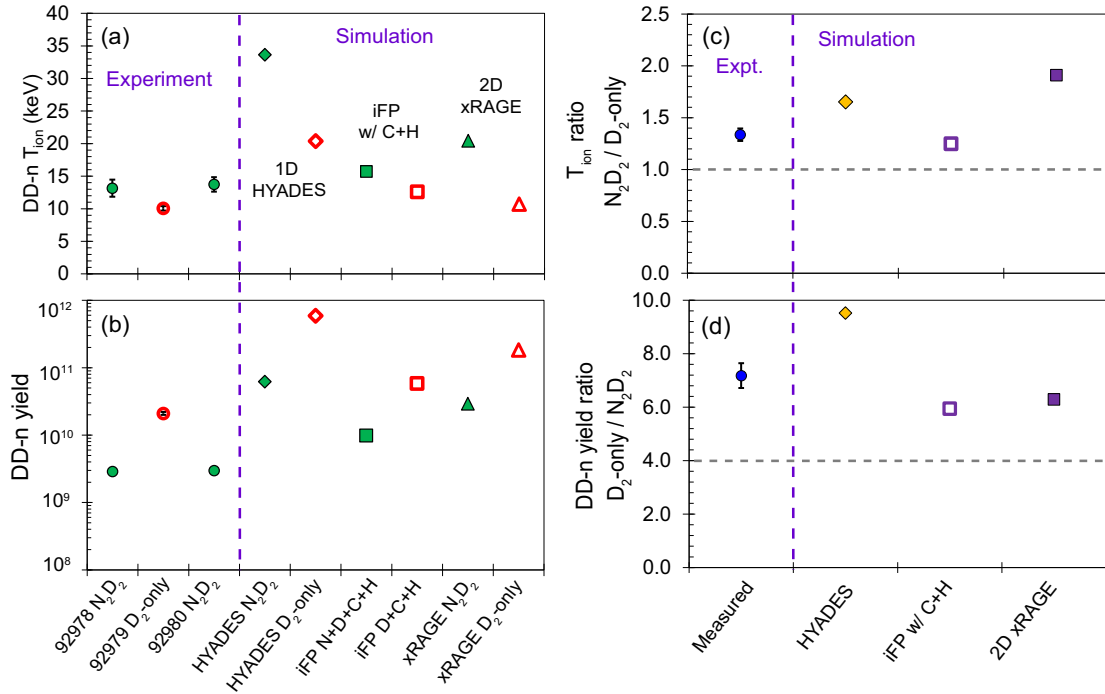


FIG. 2. Measured and HYADES, iFP, and xRAGE-simulated (a) absolute T_{ion} and (b) absolute DD-neutron yield for N_2D_2 (green solid) and D_2 -only (red open) gas-filled implosions. [(c), (d)] The same data in ratio form, with (c) the T_{ion} ratio from the N_2D_2 and D_2 -only implosions, and (d) the DD- n yield ratio from the D_2 -only and N_2D_2 implosions, with measurements (blue circles) contrasted to HYADES (yellow diamonds), iFP with C+H (open squares), and xRAGE (solid squares) simulated ratios. The gray horizontal lines represent (c) equal T_{ion} between the two implosion types and (d) the yield ratio expected due to the lower D content in the N_2D_2 fill. Measured and simulated T_{ion} are inferred from the widths of measured and synthetic DD-neutron spectra. Note that error bars are shown on the experimental data points; they are near the size of the markers.

TABLE V. 1D and 2D xRAGE-simulated yields and T_{ion} for an N_2D_2 implosion (92978) and a D_2 -only implosion (92979), respectively.

Shot	1D xRAGE yield		Standard 2D xRAGE yield		2D/1D ratio	
	Yield	T_{ion} (keV)	Yield	T_{ion} (keV)	Yield	T_{ion}
92978	1.20e11	30.0	2.91e10	20.4	24%	68%
92979	7.03e11	14.9	1.83e11	10.7	26%	72%

seeded by the 51-beam drive and the capsule stalk mount [Fig. 1(c)].

In the HYADES and xRAGE simulations, the N_2D_2 fill was treated as a single average ion species with $A = 8$, $Z = 4$. As discussed above, the interplay between the separate N and D species is expected to be important for these implosions, with predicted differential heating of N and D and subsequent heat transfer from N to D. Ion-ion mean free paths for these experiments are also inferred to be long relative to system scale size (Table III), suggesting limited validity of the hydrodynamic approximation. The versatile 1D kinetic VFP code iFP [13–18], which treats N and D separately, models interspecies diffusion, and is expected to apply when the hydrodynamic approximation breaks down, was brought to bear on the experiments to shed light on these effects. The iFP model used for these simulations includes multiple, fully kinetic ion species, but treats the electrons as a fluid. iFP has a bremsstrahlung loss term which can be turned on for the fluid electrons, but these simulations did not include this effect. The electron energy equation also does not consider viscosity. iFP does not have a laser-drive package and was initiated using output from HYADES. Initiating a kinetic simulation with output from a hydrodynamic simulation brings the questions of when in the simulation to do the handover and how sensitive the final result is to the initial conditions. To test the sensitivity to the boundary conditions, two different types of iFP simulations were performed: (i) fuel-only iFP, with the simulation initiated using the HYADES solution at the time of nearly full ionization of the fuel ions, and (ii) including some of the CH shell (iFP with <CH>, iFP with C + H), with the simulation initiated from HYADES when the ionization is close to its final value, but before the shock has traveled very far into the gas. Two different versions of the simulations including the CH shell were also run: using an averaged <CH> species, and using separate C and H species (C + H). The iFP with C + H simulations, which consider interspecies diffusion between separate N, D, C, and H species, provide the overwhelmingly best match with experimental data, and are shown contrasted to measurement in Fig. 2. Note that measured yields and T_{ion} are overestimated; this is expected because of the implosion asymmetry. Interspecies diffusion conclusions from these different ways of running iFP are discussed in detail in Sec. VI A. iFP is also used to address the dynamics of shock heating as discussed in Appendix C.

All simulations capture bang time within or nearly within error bar, demonstrating solid understanding of the overall time evolution of the implosions and the implosion velocity. Given the marginal quality of the burn history data from experiments (see Sec. II), burn width numbers are harder

to quantitatively compare. However, it should be noted that simulated numbers (Table VI) are all lower than the 130-ps number (corrected for instrumental broadening) inferred for D_2 -only shot 92979 (Table I).

V. UNDERSTANDING THE OBSERVED YIELD RATIO

As a reminder, the DD- n yield ratio between the pure D_2 and N_2D_2 -fill implosions is measured to be 7.2 ± 0.5 , which is higher than the fourfold difference expected from the difference in D content in the two implosion types alone [Fig. 2(d)]. In addition to the D content, yield also scales with the reactivity, $\langle\sigma v\rangle$, which is a strong function of T_{ion} . The $\langle\sigma v\rangle_{\text{DD}-n}$ at the measured T_{ion} for the N_2D_2 implosion of 13.5 keV is 1.9 times higher than $\langle\sigma v\rangle_{\text{DD}-n}$ at the T_{ion} for the pure D_2 implosion of 10.1 keV [58], leaving about a factor-of-4 yield difference on top of the expected due to the difference in D content remaining to be understood. In this context, note that all simulation tools brought to bear on these experiments also predict a larger difference in yield between the two fill types than the fourfold expected from D content alone, with iFP with C + H, HYADES and xRAGE simulations all capturing the measured ratio relatively closely [see Fig. 2(d)]. This motivates examining the simulations to identify the cause of the yield difference between the two implosion types.

A detailed study of the simulation output suggests that the reason for the lower yield in the N_2D_2 case, in spite of the higher T_{ion} , is that a lower fraction of the D in the fill is hot enough to burn in the N_2D_2 than in the D_2 -only implosions. This effect is large enough to dominate over the expected 1.9-fold yield enhancement due to higher T_{ion} . As will be shown below, all simulations lead to this conclusion, but for different reasons: in the kinetic simulations, the lighter D ions stream ahead of the heavier N ions with a significant fraction of the D ions predicted to have left the implosion core by the time of burn (species separation), while in the pure hydrodynamic simulations, the outer fuel layers are duded due to bremsstrahlung losses.

TABLE VI. Simulated burn widths for the N_2D_2 and D_2 -only implosions.

Fill type	Simulated burn width (ps)		
	2D xRAGE	iFP with C+H	HYADES
N_2D_2	60	83	84
D_2 only	60	76	76

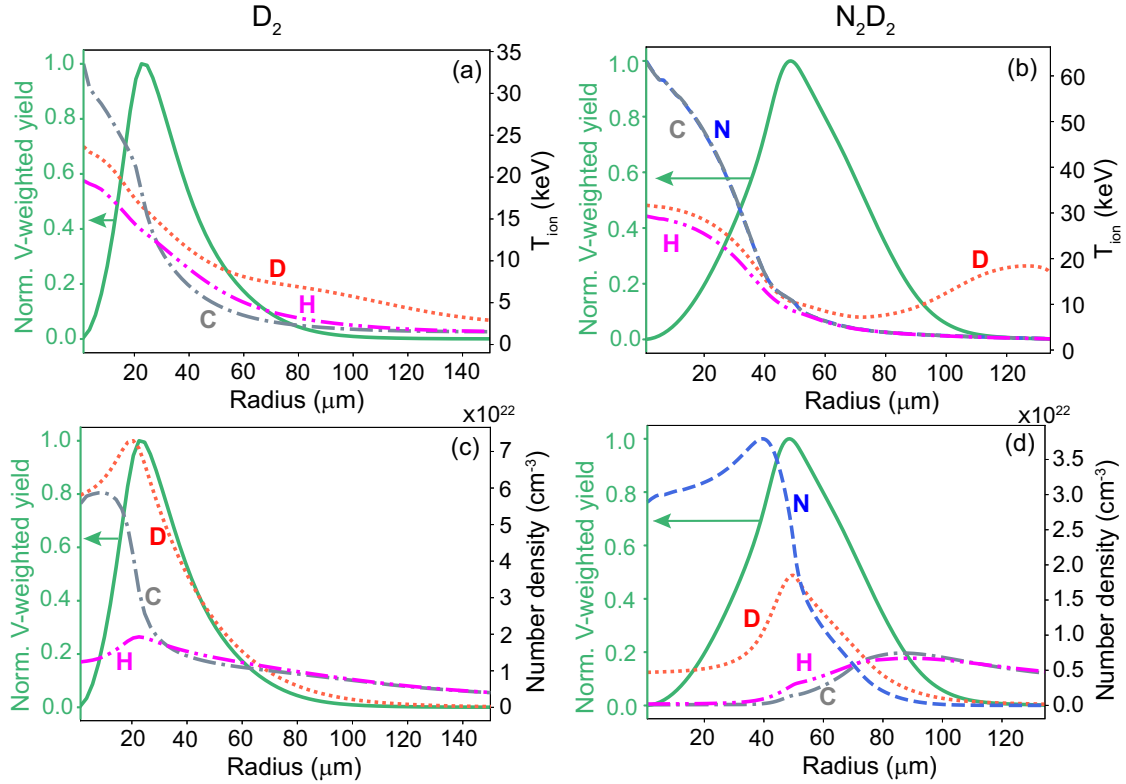


FIG. 3. iFP with C + H-simulated radial T_{ion} (top row) and ion number density (bottom row) profiles at peak burn, shown with volume-weighted, time-integrated radial burn profiles (solid green curves, left axis). [(a), (c)] Results for the D_2 -only implosions, and [(b), (d)] results for the N_2D_2 implosions. In each case, H is shown as a doubly broken purple curve; C, broken gray; D, dotted red; and N, dashed blue.

The iFP with C + H simulations consider all separate ion species and their interactions: N, D, C, and H. Bremsstrahlung is, however, not considered. iFP with C + H-simulated T_{ion} and ion number density profiles at burn for the pure D_2 and combined N_2D_2 fill implosions are shown together with the burn-averaged, volume-weighted DD- n emission in Fig. 3. As can be seen, while there is only a small difference in the D T_{ion} between the pure D_2 and combined N_2D_2 fill cases, with the latter showing higher T_{ion} consistent with measurements, there is a substantial difference in D number density, with iFP predicting that D will be largely pushed out of the hot core by the time of burn in the combined N_2D_2 fill experiment [Fig. 3(d)]. This effect, commonly referred to as species separation, is also reflected in the simulated burn profiles, with the pure D_2 -fill implosion expected to burn at a much smaller average radius than the combined N_2D_2 -fill implosion. Clearly, the reason for the lower predicted yield for the N_2D_2 mix case from iFP is removal of D from the core by burn, resulting in a lower fraction of the D burning in the combined fill compared to the pure D_2 -fill implosion. Note that the full iFP with C + H simulation is required to obtain a good match to measurements; when run in fuel-only mode, iFP appears to overestimate the mobility of the D ions; this is discussed further in Sec. VI below.

The hydrodynamic simulations also match the observed yield ratio relatively closely. This is true for both XRAGE and HYADES (see Fig. 2). HYADES, in particular, does not consider interspecies diffusion even in an approximate way.

As illustrated in Fig. 4, the HYADES simulations predict that the N_2D_2 -gas-filled implosion will converge less than the D_2 -gas-filled implosion. The lower convergence is expected due to the higher mass of the N_2D_2 versus D_2 -only fill. Still, when comparing simulated burn profiles for the two cases, the two implosion types are predicted to burn at nearly identical average radii. This can be understood by comparing the simulated T_{ion} profiles for the two cases. While the D_2 -only implosion stays hot all the way out to the fuel-shell interface, the combined N_2D_2 -fill implosion has a cold layer at the edge, indicating that bremsstrahlung coupled with radiative cooling is playing a role in this region. Radiative loss is mediated by electrons. Since τ_{ei} scales as $T^{3/2}n^{-1}$, ion cooling, mediated through radiative loss in the electron population, is expected to be stronger in this colder, denser region of the implosion, and this is indeed seen when comparing the simulated electron temperature (T_e) and T_{ion} profiles shown in Fig. 4: for the D_2 -only fill, they remain substantially different all the way out to the fuel-shell interface, while in the N_2D_2 case they converge over the last $\sim 10 \mu\text{m}$. The end result of this is that the HYADES simulations predict that a smaller fraction of the ions will be hot enough to burn in the N_2D_2 compared to the pure D_2 -fill implosion, explaining the predicted yield difference. While radiative losses are not considered in iFP and interspecies diffusion is not considered in HYADES, XRAGE does include models for both effects (but treats D and N together as an average fuel species, meaning only shell diffusion is considered

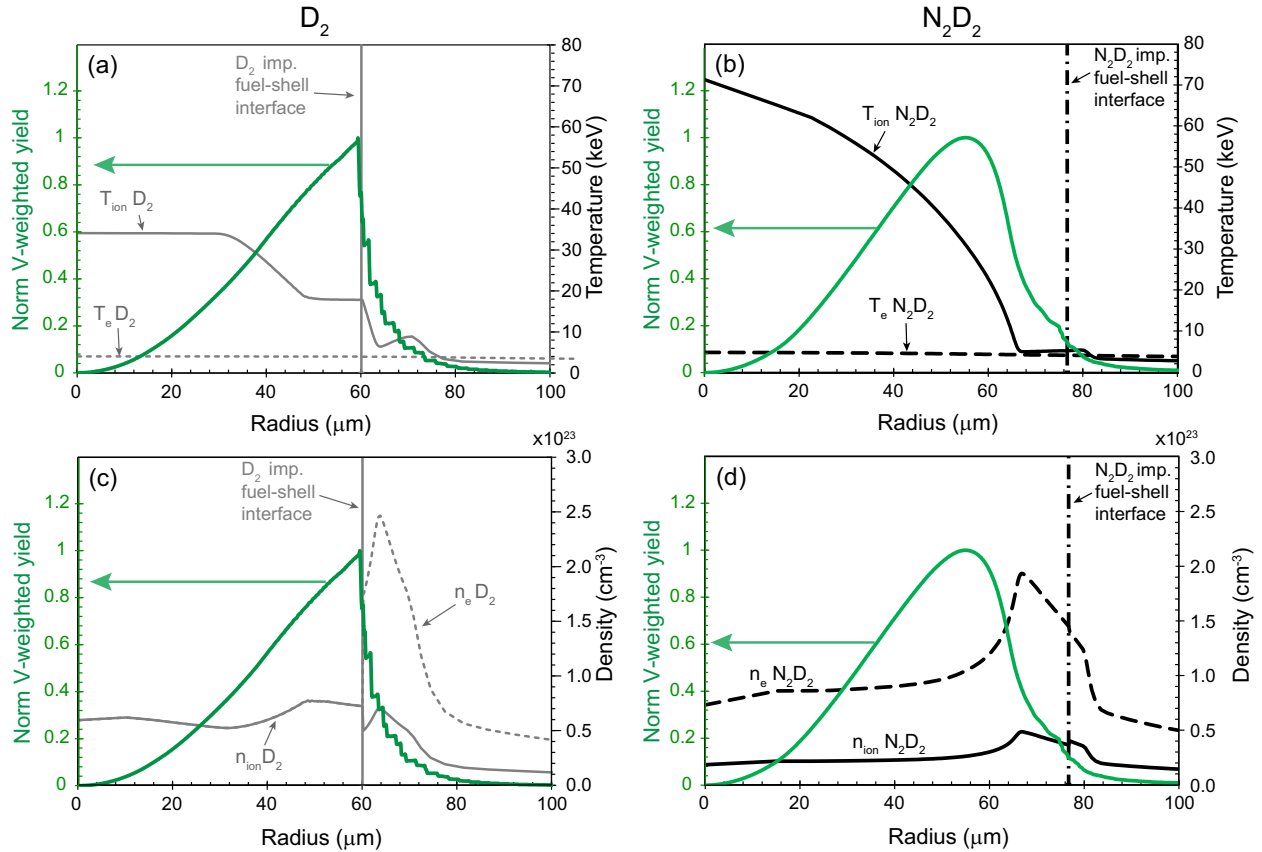


FIG. 4. 1D HYADES-simulated radial electron (dashed lines) and ion (solid lines) [(a), (b)] temperature and [(c), (d)] density profiles at peak burn (right-hand y-axis scale). Panels (a) and (c) illustrate the pure D_2 -fill and panels (b) and (d) the N_2D_2 mix-fill implosions. Also shown is the fuel-shell interface: vertical solid gray line for the D_2 -only and vertical broken black line for the N_2D_2 mix implosions. Each panel also shows the HYADES-simulated volume-weighted, time-integrated radial burn profile (green curve, left-hand y-axis), with the burn profile for the pure D_2 fill shown in panels (a) and (c) and N_2D_2 mix fill in panels (b) and (d).

with the D-N inter-ion dynamics neglected). Inspection of the XRAGE simulations suggests that both radiative losses and diffusion affect the implosions, with radiative losses penetrating deeper into the implosions when shell diffusion is considered.

Note that all simulations (VFP and hydrodynamic, Figs. 3 and 4) show substantially higher core T_{ion} for the N_2D_2 than the D_2 -only implosions and less centrally peaked deuterium densities, suggesting similar T_{ion} for the two cases and more peaked density profiles for N_2D_2 cannot explain the T_{ion} observations (compare Sec. III).

To summarize, the data from these implosions show a bigger yield difference between the pure D_2 and combined N_2D_2 -fill implosions than expected based on the difference in D content alone, in spite of the higher T_{ion} for the N_2D_2 than for the D_2 implosions, which would suggest the opposite would be expected. Such a larger yield difference effect is also predicted by all simulation tools brought to bear in this work. Kinetic iFP and hydrodynamic HYADES simulations both suggest that the difference arises due to a smaller fraction of D being hot enough to burn in the combined N_2D_2 -fill implosion, although the mechanism for this happening is different in the two cases, with the kinetic simulation showing D diffusing out of the core prior to burn, and the hydrodynamic simulation

showing the edges of the implosion dulled prior to burn due to radiative cooling. XRAGE simulations suggest both effects have a non-negligible impact.

VI. DISCUSSION

In addition to suggesting explanations for the observed yield ratio, the simulations also allow a deeper look into impact of (i) interspecies diffusion and (ii) electron viscosity in these implosions, as well as (iii) flow enhancement and (iv) nonthermal distribution impact on measured T_{ion} . These four effects are discussed in this section. Comparison of the three different iFP simulations run provides a window into the impact of interspecies diffusion, highlighting the importance of separately considering all involved ion species in the interpretation. A proposed explanation for the overestimated T_{ion} from the hydrodynamic simulations of the N_2D_2 implosions is that electron viscosity is typically neglected in these simulations, which may lead to an overestimate of ion shock heating; it is shown that this is not a significant effect for these implosions due to the large difference between T_e and T_{ion} . The discussion above claims that the observed T_{ion} difference between the N_2D_2 and D_2 -only implosions cannot

TABLE VII. iFP-simulated T_{ion} and yield for the D_2 -only and N_2D_2 implosions.

	iFP fuel only		iFP with (CH)		iFP with C+H	
Gas fill	T_{ion} (keV)	DD- n yield	T_{ion} (keV) ^a	DD- n yield	T_{ion} (keV)	DD- n yield
D_2 only	14.8	5.4×10^{11}	7.0	1.5×10^{10}	12.6	5.8×10^{10}
N_2D_2	16.1	1.2×10^{10}	21.8	1.0×10^9	15.7	9.8×10^9

^aReactivity-averaged T_{ion} (not inferred from synthetic neutron spectra as for all other reported cases).

be explained by differences in flow effect on T_{ion} in the two cases; this claim is supported by simulations compared to measurements. Additionally, the iFP simulations also allow consideration of impact of non-Maxwellian ion velocity distributions on inferred T_{ion} .

A. Impact of interspecies diffusion

There is a large and growing body of evidence suggesting that material originally in the shell diffuses into the core of an implosion on the timescale of burn [11,59–61]. Shell material diffusing into the implosion core leads to enhanced x-ray emission [61]. There are about 25 times more C atoms (in the shell) than N atoms (in the fill) in the N_2D_2 targets, suggesting that diffusion of C into the implosions and subsequent radiative loss may dominate any additional radiative loss from the added N. In this context, note that there is a significant difference in measured intensity of the softer x rays dominating time-integrated x-ray imaging between the two implosion types studied here (Appendix A), with images from the N_2D_2 implosions appearing about 75% brighter (peak emission) than the images from the D_2 -only implosions; this may suggest that shell diffusion is limited to order 1/25 of the shell in this experiment.¹ (Postprocessing of the iFP simulations gives results that also roughly agree with this simple estimate.) In addition to fuel-shell diffusion effects, separation between different ion species originally in the fuel has also been previously observed [31–33,62] and is expected to play a role in the N_2D_2 -gas-filled implosions.

The iFP code directly considers the interspecies dynamics. Studying the output from the iFP simulations in detail, the relative ion dynamics are seen to be dominated by free streaming of the fastest ions in each individual ion population. As mentioned in Sec. IV, iFP was run in three different ways as part of this work: fuel only (not considering the CH shell), approximating the CH shell as an average ion with $Z = 3.5$ and $A = 6.5$ (iFP with (CH)), and considering the shell as separate C and H ion species (iFP with C + H). T_{ion} and yield results from all three runs are contrasted in Table VII. The iFP with C + H simulations provide a reasonably good match

to measured absolute T_{ion} as well as yield and T_{ion} ratios (compare Fig. 2). In contrast, both the fuel-only and iFP with (CH) simulations overestimate the yield ratio at 45 times and 15 times, respectively. As discussed in Sec. V, the measured yield ratio is well explained by a lower fraction of the D being hot enough to burn in the N_2D_2 versus D_2 -only implosions. Figure 5 contrasts the T_{ion} and number density profiles at bang time for the three different iFP simulation configurations. Comparing the iFP with C + H number density profiles with those from the fuel-only and with (CH) iFP simulations, it is clear that the difference in D density in the core for the D_2 -only versus the N_2D_2 case is highest for the fuel-only simulations, reduced for iFP with (CH), and lowest for iFP with C + H. These relative density differences explain the yield ratio differences observed among the three simulations and are a result of the interspecies dynamics. The lighter the ion species, the higher its relative mobility. For the fuel-only simulation [Figs. 5(a) and 5(e)], the D species is much more mobile than N, with N pushing D out of the core by the time of burn (i.e., the lighter D essentially free-streaming through the heavier N species). For the (CH) simulation [Figs. 5(b) and 5(f)], the average CH species contributes to pushing D out of the core for both the D_2 -only and N_2D_2 cases. The end result is a smaller difference in D density at burn between the two implosion types, and a closer match with measurement. When C and H are considered as separate species, C and N have comparable mass and mobility, while H is lighter than D and contributes to holding D back, relatively speaking. This consequently leads to higher D number densities at burn than for the (CH) case, and to a smaller difference in ion number density between the two implosion types. Given the much better match with the measured yield ratio for the iFP with C + H than for the other two simulations, it appears that the fuel-only and (CH) simulations overestimate D mobility, whereas separately considering all ion species more closely captures the experimental observables. It should be noted that the iFP with C + H simulations suggest that shell (specifically C ion) mix penetrates deeper into the implosion for the D_2 -only than for the N_2D_2 case by the time of burn. This could be consistent with the experimentally observed difference in x-ray brightness assuming the N dominates radiation in the N_2D_2 case, but this topic will be the subject of more detailed study with differentially filtered x-ray imaging in future experiments.

The heavier ion species reach higher T_{ion} in iFP as expected; this is seen in the T_{ion} profiles in Fig. 5. As a reflection of interspecies equilibration effects, these differences reduce and eventually disappear at later times in the implosion. The time

¹This number is obtained by assuming the x-ray emission scales with the total number (N) of electrons in the core: $N_{e,\text{N}_2\text{D}_2}/N_{e,\text{D}_2} = 1.75 = (N_{\text{D},\text{N}_2\text{D}_2} + 7N_{\text{N},\text{N}_2\text{D}_2} + 6N_{\text{C},\text{N}_2\text{D}_2})/(N_{\text{D},\text{D}_2} + 6N_{\text{C},\text{D}_2})$. Using the fact that $N_{\text{D},\text{N}_2\text{D}_2} = N_{\text{N},\text{N}_2\text{D}_2} = 0.5N_{\text{D},\text{D}_2}$ and assuming $N_{\text{C},\text{N}_2\text{D}_2} = N_{\text{C},\text{D}_2} = \text{const} \times N_{\text{D},\text{D}_2}$, it is concluded that $N_{\text{C},\text{N}_2\text{D}_2} \approx N_{\text{N},\text{N}_2\text{D}_2}$, i.e., $\sim 1/25$ of the C known to be in the shell.

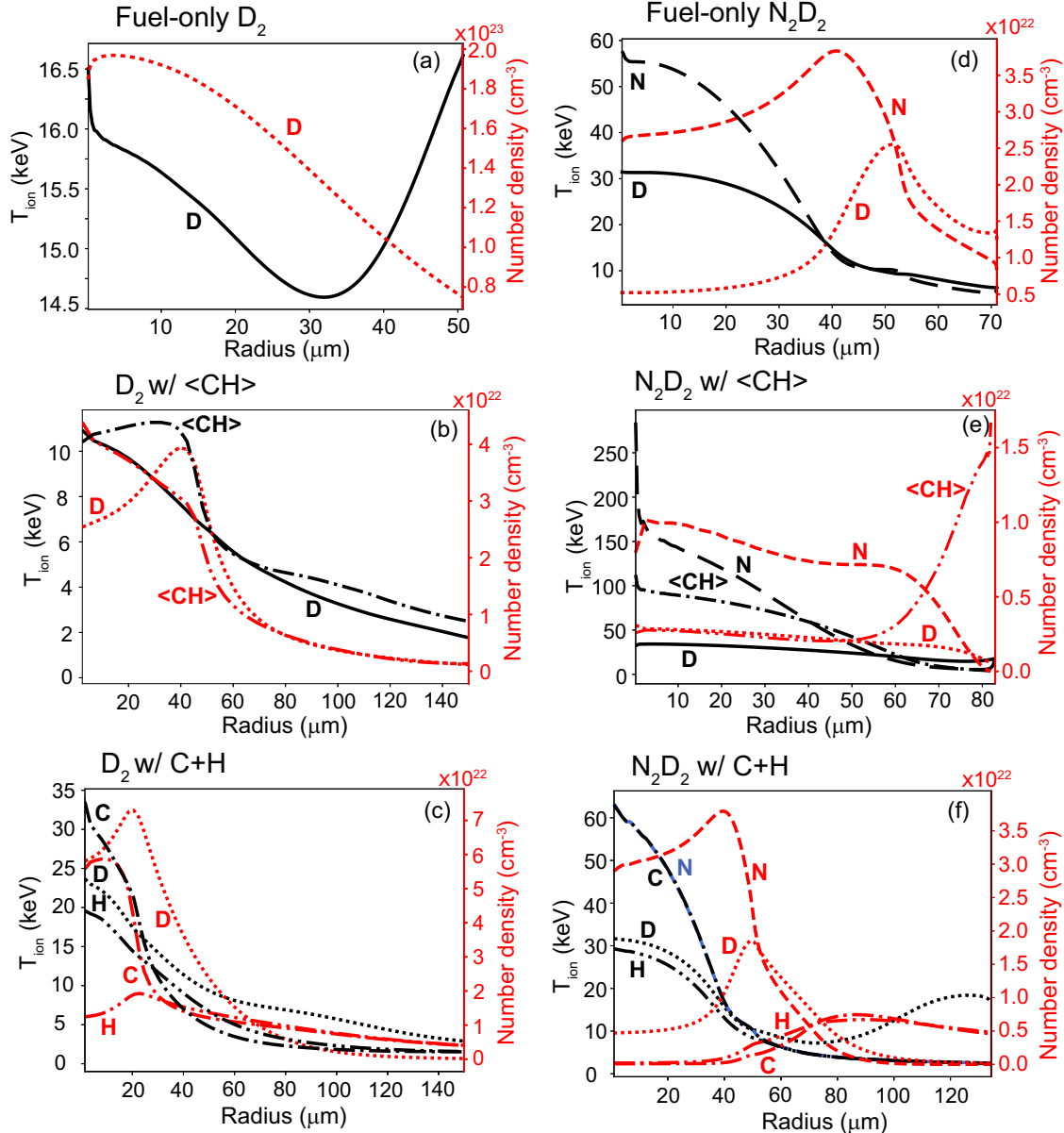


FIG. 5. iFP-simulated T_{ion} and number density profiles [(a), (d)] without the CH shell, [(b), (e)] with the CH shell considered as an average (CH) ion (iFP with (CH)), and [(c), (f)] with the CH shell considered as separate C + H ion species (iFP with C + H). [(a)–(d)] The D_2 -only case, [(e)–(h)] the N_2D_2 case.

evolution of temperature for the different particle species is discussed further in Appendix C.

An area of uncertainty in the iFP simulations concerns the point at which the simulation is initiated from HYADES. The initial conditions for the fuel are very far from equilibrium at the beginning of all iFP simulations, with extremely large N_k near the shock front at $> \sim 10$. It is clear from Fig. 5 and Table VII that the treatment of the shell can have a significant impact on the end result. Ideally, a kinetic code should handle this self-consistently by including the laser drive, which would eliminate this problem.

B. Impact of electron viscosity

As seen in Sec. IV, the hydrodynamic simulations substantially overestimate T_{ion} for the N_2D_2 implosions. It has been suggested that this could be because these simulations neglect electron viscosity. Velikovich *et al.* [63] suggested that neglecting electron viscosity could lead to overestimated shock heating, in particular with higher-Z ions involved; such an effect was also suggested as an explanation for overpredicted shock burn in xRAGE simulations of recent OMEGA data [64]. This effect has been recently implemented in the xRAGE code. Table VIII compares results from running xRAGE in three

TABLE VIII. Results from running xRAGE in three different ways: standard without viscosity, with plasma viscosity, and with plasma viscosity considering shock splitting between electrons and ions.

	Yield ratio	N ₂ D ₂ T_{ion} (keV)	D ₂ T_{ion} (keV)	N ₂ D ₂ burn width (ps)	D ₂ burn width (ps)
Standard xRAGE (no viscosity)	6.28	20.44	10.71	60	60
xRAGE with plasma viscosity	5.49	21.24	10.72	70	80
xRAGE with plasma viscosity and shock splitting	5.76	21.19	10.73	70	70

different configurations: (i) without considering viscosity, (ii) with plasma viscosity, and (iii) with plasma viscosity and considering Velikovich shock splitting, i.e., allowing energy from the shocks to split between ions and electrons due to finite electron viscosity. As can be seen in Table VIII, while considering real plasma viscosity has some minor impact on the simulation results, also considering electron viscosity has negligible additional impact. Studying the simulations in detail, it is concluded that this result makes sense; electron viscosity is indeed negligible for these implosions. Shock splitting will only matter if the electron viscosity is comparable to ion viscosity. With the electron-to-ion viscosity ratio scaling as $(m_e/m_i)^{1/2}Z^3(T_e/T_{\text{ion}})^{5/2}$, the high Z in the N₂D₂ case leads to the prediction of a significant effect; the reason it is not seen is because $T_{\text{ion}} \gg T_e$ for these implosions.

C. Impact of flow on T_{ion}

As briefly mentioned in Sec. III, T_{ion} as inferred from neutron spectra will include a contribution from any plasma flows during burn [43–48], including isotropic radial flow and anisotropic directional flow. In this section, the expected impact of flows on T_{ion} inferred from the present experiments is addressed with the aid of the simulations described in Sec. IV. While these effects will impact apparent T_{ion} , they cannot explain the observed T_{ion} difference between the N₂D₂ and D₂-only fill, and hence do not invalidate the conclusion of stronger heating with N in the fuel.

1. Radial flow

Isotropic radial motion of the fuel at burn leads to a broadening of the neutron spectrum inseparable from thermal broadening in the measurement [46]. However, substantial radial motion (on the order of hundreds of km/s) is required to significantly increase inferred T_{ion} . Figure 6 shows iFP with C + H-simulated radial D velocity profiles at bang time and burn-weighted D velocities as a function of time for the D₂-only and N₂D₂ implosions. Burn-averaged radial flow velocities of 265 km/s for D₂-only and 135 km/s for the N₂D₂ implosions are inferred. This suggests the D₂-only-measured T_{ion} is more inflated by flow than the N₂D₂-inferred T_{ion} ; the numbers suggest about ~ 0.55 keV expected difference in inferred T_{ion} between the two implosion types due to flows, which, assuming iFP is accurately describing the experiments, would increase the T_{ion} difference from 34% to 45%. (While radial flows thus do not account for the observed T_{ion} difference, this is not an insignificant effect and clearly should be considered in the interpretation of results.) Postprocessing of

HYADES output also leads to the conclusion that radial flows cannot explain the observed T_{ion} difference (see Appendix D).

2. Directional flow

Radial flow can thus be ruled out as a substantial factor influencing relative T_{ion} in these implosions. However, given the substantial asymmetry seeded by the asymmetric drive as illustrated in Fig. 1, directional flows must also be considered. Such directional flows manifest as variations in T_{ion} inferred along different lines of sight (LOS) around an implosion (see, e.g., Refs. [46–48,65]). The first thing to note here is that the asymmetry direction in these experiments is consistent between the implosion types (see Fig. 10 in Appendix A). This means that if there was a LOS enhancement in T_{ion} due to directional flow, it would be expected to arise in a systematic fashion for the different implosions. The nTOF in the $\theta, \varphi = 116.57^\circ, 162^\circ$ LOS used to measure T_{ion} from these experiments also has the capability of inferring directional flow through measurement of the shift in mean peak energy of the DD neutrons [66,67]. The measured directional-flow results are illustrated in Fig. 7. The $\theta, \varphi = 116.57^\circ, 162^\circ$ LOS is about 100° removed from the direction of the weak spot in the laser drive. Assuming the maximum flow is in the direction of the weak spot, a -50 km/s measured flow along $\theta, \varphi = 116.57^\circ, 162^\circ$ would suggest a maximum flow of $50/\cos 100^\circ = 288$ km/s. As can be seen, similar flows are inferred for all three implosions.

To understand the possible impact of such directional flows on inferred T_{ion} , it is illustrative to study the 2D xRAGE simulations, which, as a reminder, do consider the imposed drive asymmetry, but in a simplified geometry with the stalk and drive weak spot directly opposing each other. (Comparison of measured and synthetic xRAGE-generated time-resolved x-ray images suggest that xRAGE does indeed overestimate the asymmetry, while capturing its general features well. See Appendix A.) The xRAGE-calculated directional flows parallel and perpendicular to the imposed asymmetry are summarized in Table IX along with T_{ion} inferred from synthetic neutron spectra in the two directions. The maximum flows (inferred along the asymmetry direction) are higher than estimated from the data in Fig. 7; this is to be expected given the simplified 2D geometry in the simulation. However, even with these overestimated flows, T_{ion} is not substantially impacted, with expected LOS differences < 0.61 keV, allowing us to rule out directional flows as the source for the T_{ion} anomaly.

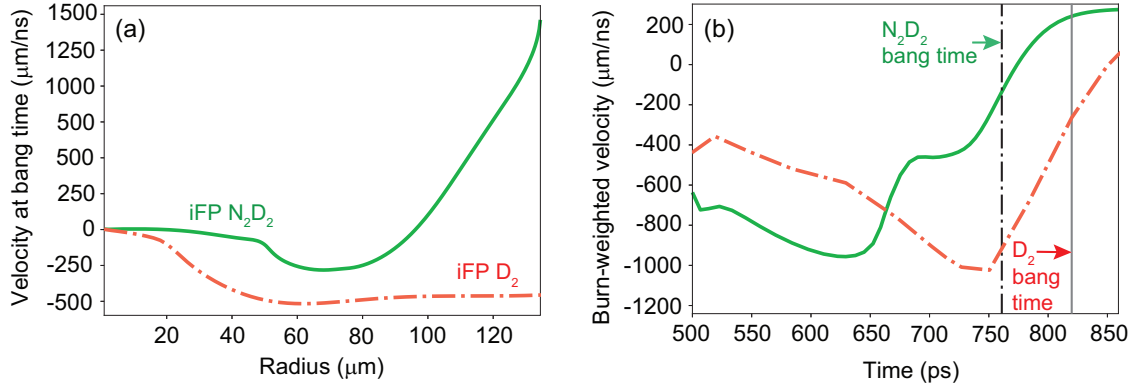


FIG. 6. C+H iFP-simulated D velocity (a) at bang time and (b) burn-weighted vs time for the D_2 -only (broken red curves) and N_2D_2 fill (green solid curves) implosions.

D. Impact of non-Maxwellian ion-velocity distributions

The standard experimental T_{ion} analysis assumes Maxwellian velocity distributions of the reacting ions [42]; if the ion-velocity distributions are non-Maxwellian, the relationship between T_{ion} and the neutron spectrum broadening is different compared to the Maxwellian case [68]. A method for directly calculating synthetic neutron spectra from iFP-simulated ion distributions, which are self-consistently evolved without any imposed constraints, has been recently developed [69], which allows the effect of non-Maxwellian ion-velocity distributions on neutron spectra to be studied. The T_{ion} values of 12.59 keV (15.71 keV) for the D_2 and N_2D_2 iFP with C + H simulations (shown in Table VII) are inferred from the width of the simulated DD- n spectra using this method. If instead the spectra are calculated assuming a local Maxwellian with temperature equivalent to the mean energy of the iFP-simulated ion-velocity distributions, then values of 13.4 keV (15.65 keV) are obtained. The iFP simulations suggest that the underlying

ion-velocity distributions for the present experiments deviate from Maxwellian, in particular for the D_2 -only case. The comparison between the two calculations indicates that the non-Maxwellian effects generated by the shock can have an impact on experimental observables. Note, however, that apparent T_{ion} is inferred in exactly the same way from the measurements and from the iFP simulations; while further work is required to understand the relationship between reactivity and apparent T_{ion} when such effects are present, the comparisons made in this paper remain valid.

VII. CONCLUSIONS

Thin plastic shell implosions with 100% D_2 gas fill compared to 50:50 N_2D_2 gas fill at the same total number density, executed at the OMEGA laser facility, demonstrate $34\% \pm 6\%$ higher deuterium T_{ion} for the N_2D_2 gas-fill implosions, and 7.2 ± 0.5 times higher DD-neutron yield for the pure D_2 -fill implosion. The T_{ion} enhancement for the N_2D_2 case is observed in spite of higher Z in these implosions, which might suggest enhanced radiative cooling, and in spite of weaker shocks relative to the D_2 -only case. At the same time, the yield for the D_2 -only implosions is higher than the yield from the N_2D_2 implosions by more than the factor of 4 expected from the difference in D content alone. These results are understood in terms of enhanced shock heating of N compared to D, heat transfer from N to D on the timescale of the implosion (for the added heating to be observed in the deuterium T_{ion}), and limited additional radiative loss due to the N in the fuel prior to burn. Equilibration times calculated from

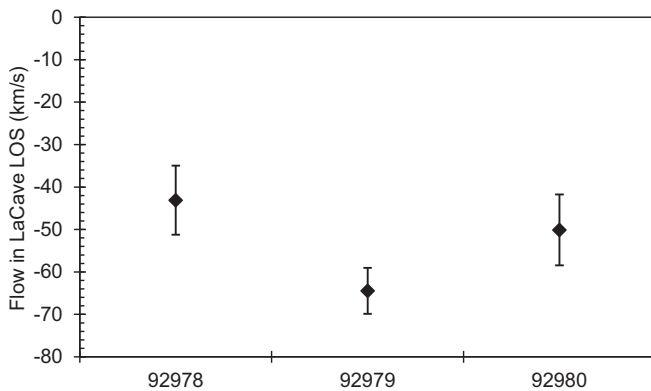


FIG. 7. Directional flow as measured along the $\theta = 116.57^\circ$, $\varphi = 162^\circ$ direction, 100° from the known weak spot in the laser drive. The flows are inferred from the downshift in mean energy of measured DD-neutron spectra. On average, these measured flows are consistent with a velocity of ~ 300 km/s in the direction of the laser drive weak spot. See text for further details.

TABLE IX. 2D xRAGE-simulated directional flows, and their impact on inferred T_{ion} . (Note that dir 0 0 1 is upward in the view in Fig. 10 in Appendix A, while dir 1 0 0 is to the right.)

	92978 (N_2D_2)	92979 (D_2 only)
Flow in 0 0 1 dir (km/s)	-450.76	-601.52
Flow along 1 0 0 dir (km/s)	-36.36	-23.73
Apparent T_{ion} along 0 0 1 (keV)	21.19	11.34
Apparent T_{ion} along 1 0 0 (keV)	20.92	10.73

observables support this picture; the N-D equilibration time (τ_{ND}) is indeed short enough to allow heat transfer and the N-*e* equilibration time (τ_{Ne}) long enough where the electron population bremsstrahlung heat loss cannot be expected to fully propagate to the ions prior to burn. In addition, $\tau_{ND} \gg \tau_{Ne}$, suggesting N will transfer heat to D faster than losing it to the electrons.

Kinetic and hydrodynamic simulations both predict a yield loss for N_2D_2 versus D_2 -only implosions by more than the factor of 4 expected from the difference in D content alone, consistent with the experimental observation. In both types of simulations, the enhanced yield loss is due to a lower fraction of the D fuel being hot enough to burn in the N_2D_2 -gas-filled implosions compared to the D_2 -only case, but the underlying physics are different between the hydrodynamic and kinetic pictures. In the kinetic simulations, the reduced yield is due to deuterium streaming out of the imploding core prior to burn, with the heavier ion species (N and/or C) instead concentrating in the core. Comparison of iFP simulations considering (i) the fuel only, (ii) the shell as an average (CH) species, and (iii) the shell as separate C + H species show that the former two approximations overestimate D diffusion out of the core and hence the measured yield ratio of D_2 only to N_2D_2 . Considering C and H as separate species allows the lighter H species to contribute to holding D back, relatively speaking, and provides a much closer match with experimental observables.

In the hydrodynamic HYADES simulations, the additional yield loss arises because of enhanced radiative loss due to bremsstrahlung coupled with ion-electron equilibration at the cooler, denser, outer edges of the implosion. Experimentally, and as suggested by xRAGE simulations, which include both radiative losses and an approximate model for diffusion (considering shell diffusion but not N/D inter-ion dynamics), the most likely scenario is that both effects contribute. The HYADES simulations predict similar burn radii for the two implosion types, while the kinetic simulations predict that the N_2D_2 implosions will burn at a larger average radius; future experiments where the nuclear burn radius is measured could help shed light on the relative importance of the two effects.

All simulations overestimate measured absolute yield and T_{ion} . A comparison between 1D and 2D xRAGE-simulated yields and T_{ion} shows a factor-of-4 impact on yield and 30% impact on T_{ion} of considering the higher dimensionality in the simulations; this suggests that multidimensional effects strongly contribute to the performance overprediction.

The hydrodynamic simulations overestimate T_{ion} for the N_2D_2 implosions. This work considered, and ruled out, shock splitting between ions and electrons with non-negligible electron heating as an explanation for this. Small differences between xRAGE simulations considering versus not considering electron viscosity suggest minimal impact of this effect on these implosions; electron viscosity will only matter if it is comparable to ion viscosity, and it is not for these implosions because $T_{ion} \gg T_e$ (however, this is an interesting avenue for future investigation, in particular for higher-*Z* fill implosions with lower T_{ion}). Instead, the overestimated N_2D_2 T_{ion} in the hydrodynamic simulations is concluded to be due to the multi-ion effects of enhanced shock heating of N and subsequent equilibration with D not being captured, with the two species

being treated as a single average species with $A = 8$ and $Z = 4$.

Comparison of measured and simulated T_{ion} and flows shows that flows have a small impact on T_{ion} inferred from DD-neutron spectra (<1 keV T_{ion} inflation), not sufficiently different between the D_2 -only and N_2D_2 cases to affect the conclusion of stronger heating with N added in the fuel.

Detailed postprocessing of the iFP simulations shows that assuming Maxwellian ion-velocity distributions does have an effect on inferred T_{ion} compared to considering the full simulated ion-velocity distributions. These iFP results do identify the effect of non-Maxwellian ion-velocity distributions on inferred neutron spectra as a crucial area of further research; since a long-term goal is to use this platform for S-factor measurements relevant to nuclear astrophysics, it is critical to understand the relationship between reactivity and apparent T_{ion} when such effects are present. Such work has already started, including as discussed in Refs. [70,71].

The purpose of the experiments described herein was to test feasibility of developing this platform for the study of low-probability, mid-*Z* nuclear reactions relevant to nuclear astrophysics, as an extension of the low-*Z* ICF platform for this purpose described in Refs. [1,2]. In particular, the long-term goal of this work is to facilitate studies of CNO-relevant reactions in a plasma environment. The T_{ion} and yield results obtained, with higher T_{ion} observed with the addition of N in the gas fill with less than two times additional loss in yield compared to expected based on D content difference alone, mean that the platform meets the first necessary requirements suggesting it can be developed for this purpose. However, further study of the plasma conditions achieved will be required before firm conclusions regarding the utility of the platform for such experiments can be reached.

ACKNOWLEDGMENTS

The authors sincerely thank the OMEGA operations staff who supported this work. This material is based upon work supported by the Department of Energy, National Nuclear Security Administration under Awards No. DE-NA0003868 and No. DE-NA0003938. This work was supported by the Laboratory Directed Research and Development program of Los Alamos National Laboratory for W.T.T. Sandia National Laboratories is a multimission laboratory managed and operated by National Technology & Engineering Solutions of Sandia, LLC, a wholly owned subsidiary of Honeywell International Inc., for the U.S. Department of Energy's National Nuclear Security Administration under Contract No. DE-NA0003525.

This report was prepared as an account of work sponsored by an agency of the U.S. Government. Neither the U.S. Government nor any agency thereof, nor any of their employees, makes any warranty, express or implied, for the accuracy, completeness, or usefulness of any information, apparatus, product, or process disclosed, or represents that its use would not infringe privately owned rights. Reference herein to any specific commercial product, process, or service by trade name, trademark, manufacturer, or otherwise does not necessarily constitute or imply its endorsement, recommendation, or favoring by the U.S. Government or any agency thereof.

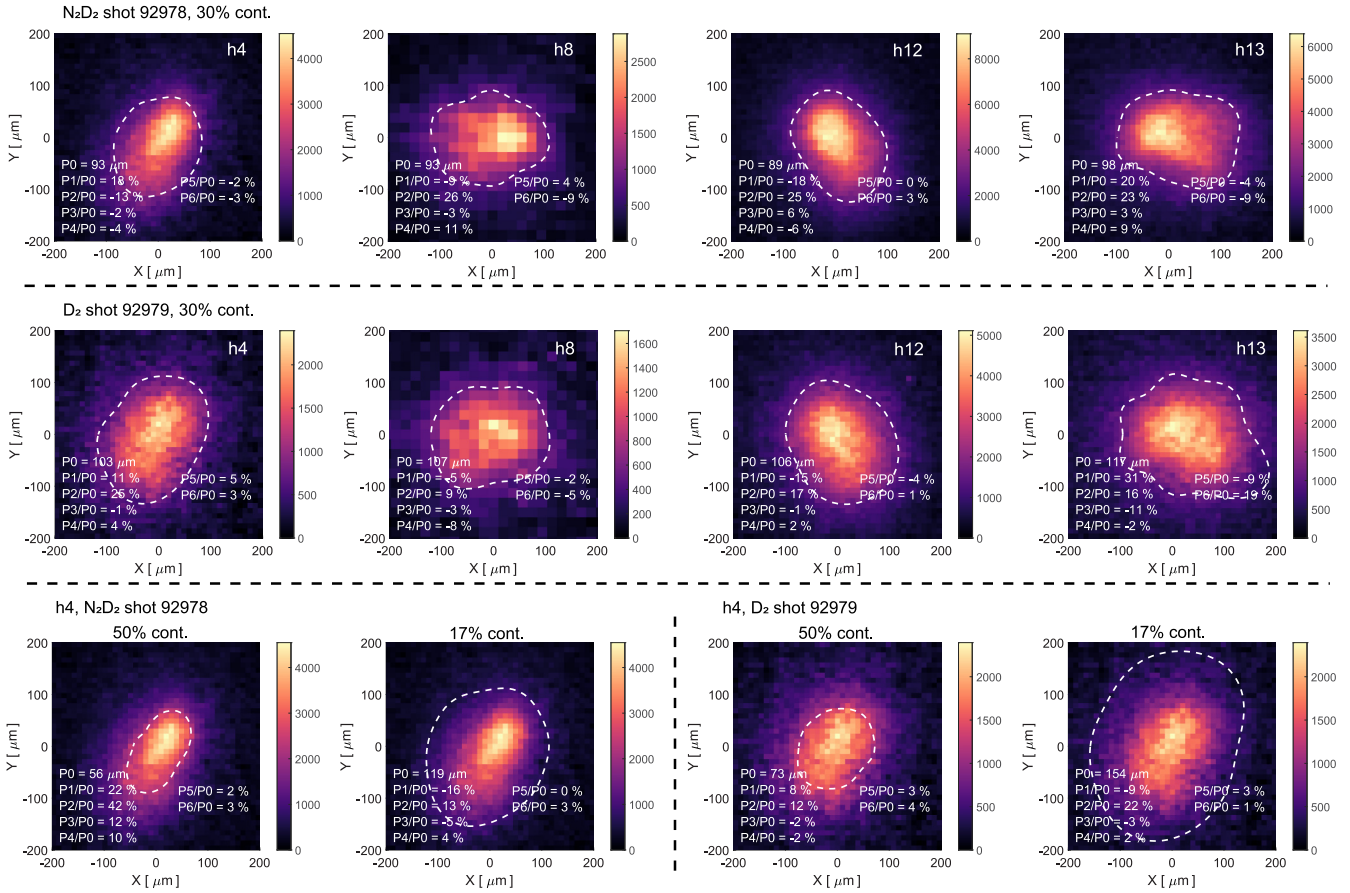


FIG. 8. Measured time-integrated x-ray pinhole camera images in four LOS (OMEGA ports h4, h8, h12, and h13) from shots 92978 (N_2D_2 fill) and 92979 (D_2 fill). The intensity scale represents counts on the CCD used to record the images. The peak intensity observed on shot 92978 is $\sim 75\%$ higher on average compared to shot 92979. Also shown are contour fits to the data. For h4, three different x-ray intensity level contour fits are shown: 17%, 30%, and 50% of peak intensity. The 30% contour fits appear to best capture the measured signatures. There is an obvious asymmetry due to the asymmetric drive on these experiments, which is clearly reproducible between the two implosions.

The views and opinions of authors expressed herein do not necessarily state or reflect those of the U.S. Government or any agency thereof.

APPENDIX A: IMPLOSION SIZE

An estimate of implosion size is required to calculate an empirical number density for use in the equilibration time and K_r calculations presented in this paper. Since these quantities are averaged over burn, the size of the burning region is desired. However, no nuclear emission imaging data were obtained from these implosions. Instead, time-resolved and time-integrated self-emission x-ray imaging measurements are used to infer implosion size. Time-integrated x-ray images were obtained with five different instruments distributed around the target chamber; four of these [the x-ray pinhole (XRPH) cameras] used 150 μm Be and 100 μm Al filtering, 1 ns integration time, and CCD detectors to measure x rays with energy >5 keV, while the fifth used 15 μm Ta and 1500 μm CR-39 filtering and an image plate detector to mea-

sure x rays with energy >20 keV. The time-resolved images were obtained using a pinhole array and a framing camera filtered with 25 μm Be and fielded at polar, azimuthal angle $\theta = 142.62^\circ$, $\varphi = 342^\circ$, to obtain images with 35 ps integration time and at x-ray energies >1 keV.

Examples of time-integrated x-ray images measured with the XRPH cameras are shown in Fig. 8. There are a few things that should be noted about these images. First, the measured data exhibit substantial asymmetry, as expected from the asymmetric laser drive used in these experiments. This is clear from the images obtained at different angles using XRPH cameras h4, h8, h12, and h13, respectively, shown in the top two rows of Fig. 8. However, this asymmetry has a minor impact on overall inferred implosion size, as evidenced by the comparison of inferred fuel radii from the different viewing directions, and is also highly consistent between the different implosions. Second, no substantial difference in inferred image size is seen between the N_2D_2 and D_2 -only implosions (see also Fig. 9), although considering all the contour level fits, the D_2 -only implosion appears slightly larger than the N_2D_2 implosions. Third, there is a clear difference in peak image intensity observed between the implosions, with

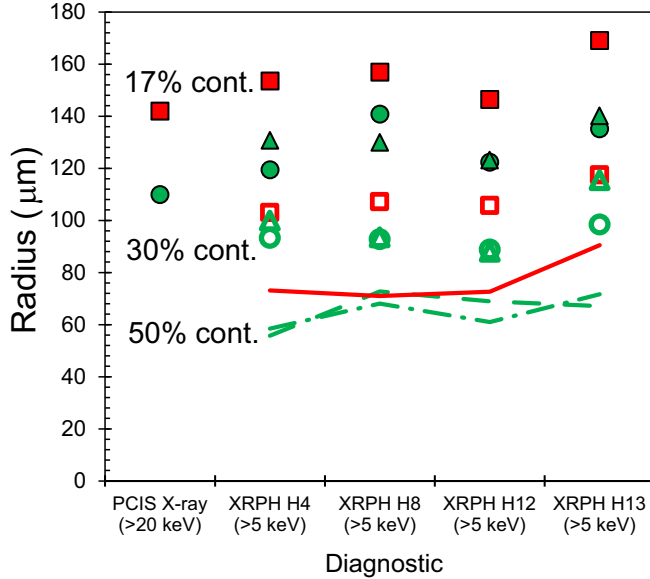


FIG. 9. Implosion radii inferred from time-integrated x-ray images (Fig. 8), with N_2D_2 shot 92978 shown as green circles and dashed curve, N_2D_2 shot 92980 as green triangles and dash-dotted curve, and D_2 -only shot 92979 shown as red squares and solid curve. The implosion size is inferred from fits to the 17% intensity contour (solid symbols), 30% intensity contour (open symbols), and 50% intensity contour (curves), respectively, with progressively smaller radii inferred for the higher-intensity contours. For the purposes of this paper, the best-estimate burn radius is taken from these data to be $100 \pm 40 \mu\text{m}$.

the images from N_2D_2 shot 92978 showing on average $\sim 75\%$ higher peak intensity than the images from D_2 shot 92979 (this conclusion also holds for the other N_2D_2 shot, 92980). Finally, the inferred implosion size is affected by how the image is analyzed. Figure 8 also shows three different contour level fits to the h4 camera data: 17%, 30%, and 50%. Going from 17% to 50%, the inferred implosion size decreases by about a factor of 2. Figure 9 displays the quantitative results from the various contour fits. In addition to the inferred radii resulting from the fits shown in Fig. 8, fit results for remaining camera positions and shots are also shown. Note that the radii inferred from the fits to the final x-ray camera, only observing x rays above 20 keV, are only very slightly lower than the results from the >5 keV camera fits.

The crucial question is which contour level fit best represents the size of the burning fuel. This cannot be directly determined from the data. However, studying Fig. 8, the 30% contour fits do appear to best capture the signatures in data, suggesting that a realistic estimate is $\sim 100 \mu\text{m}$ radius. An upper limit of $140 \mu\text{m}$ is set by the 17% contour fits and a lower limit of $60 \mu\text{m}$ by the 50% contour fits. Note in this context that iFP-inferred nuclear burn radii (Fig. 3) are smaller than $100 \mu\text{m}$. The HYADES simulations show burn out to $100 \mu\text{m}$, but with an average nuclear burn radius of $\sim 50 \mu\text{m}$ for both implosion types (Fig. 4). Thus, while a total burn radius of $100 \mu\text{m}$ may be reasonable, simulations suggest most of the burn is happening within the inner $60 \mu\text{m}$.

Example time-resolved images from N_2D_2 shot 92978 and D_2 -only shot 92979 are shown in Fig. 10, and contrasted to synthetic images from the 2D xRAGE simulations for shot 92978. Looking at the measured images, there is no obvious difference in size between shots 92978 and 92979 (such images, obtained from x-ray framing cameras, are not interpreted absolutely because small changes in bias voltage can lead to large differences in signal levels). The signatures of the stalk mount (lower left corner) and region of reduced laser drive (lower right corner) can both be clearly observed at all times, with the weak spot of the drive apparently leading to jetting at later times, with three distinct bright spots appearing in the second image for both 92978 and 92979 [these bright spots appear to correlate with the spots of weakest drive appearing in the VisRad-simulated laser drive distribution shown in Fig. 1(b)]. Standard analysis methods for this type of image fail even at early times due to the “fuzzy” edges in the images. However, the images are plotted on a target plane scale, and the overall bright spot can be seen to range from $\sim 800 \mu\text{m}$ diameter at early times to roughly $400 \mu\text{m}$ at late time. The images from the 2D xRAGE simulations show an asymmetry clearly reminiscent of the asymmetry in the measured data, although exacerbated at late times and not directly comparable due to the limitations of the 2D xRAGE geometry: as a reminder, the xRAGE simulations consider the stalk mount and laser drive weak spot, but with these features at 180° angle to each other, versus 137° in the experiment (in the Fig. 10 view, the stalk is at the top in the xRAGE images, while the drive weak spot is at the bottom). Synthetic xRAGE images from 0.4 to 0.65 ns have been analyzed for shell radius using the method described in Ref. [72], with inferred shell radii ranging from $\sim 375 \mu\text{m}$ at 0.4 ns for both implosions to $180 \mu\text{m}$ for D_2 only and $200 \mu\text{m}$ for N_2D_2 at 0.65 ns. This roughly agrees with the radii inferred from inspection of the measured data at these times. The time-resolved x-ray images provide no reason to change the conclusion of a burn radius of $100 \pm 40 \mu\text{m}$ as inferred from the time-integrated images above.

APPENDIX B: LOCAL VARIATIONS IN τ_{ei} AND N_k

Burn-averaged numbers for equilibration times and N_k are calculated in Secs. III A and III B. Given large density and temperature variations as a function of time and space (see, e.g., Figs. 3 and 4), it is clear that significant local variation in these numbers is expected.

As an example, Fig. 11 shows the nitrogen ion-electron equilibration times τ_{ei} calculated from the HYADES N_2D_2 implosion simulations as a function of radius at bang time and (in steps of 10 ps) up to 50 ps before bang time. Not unexpectedly, large variations in this quantity over time and space are observed, with the shortest τ_{ei} observed at bang time and in the denser regions near the fuel-shell interface. Overall, the experimentally inferred average number of 55 ps (Table II) appears in good agreement with that expected from the simulation. The equilibration observed in the outer region of the implosion in the HYADES T_i and T_e profiles at bang time (Fig. 4) is also consistent with these calculations.

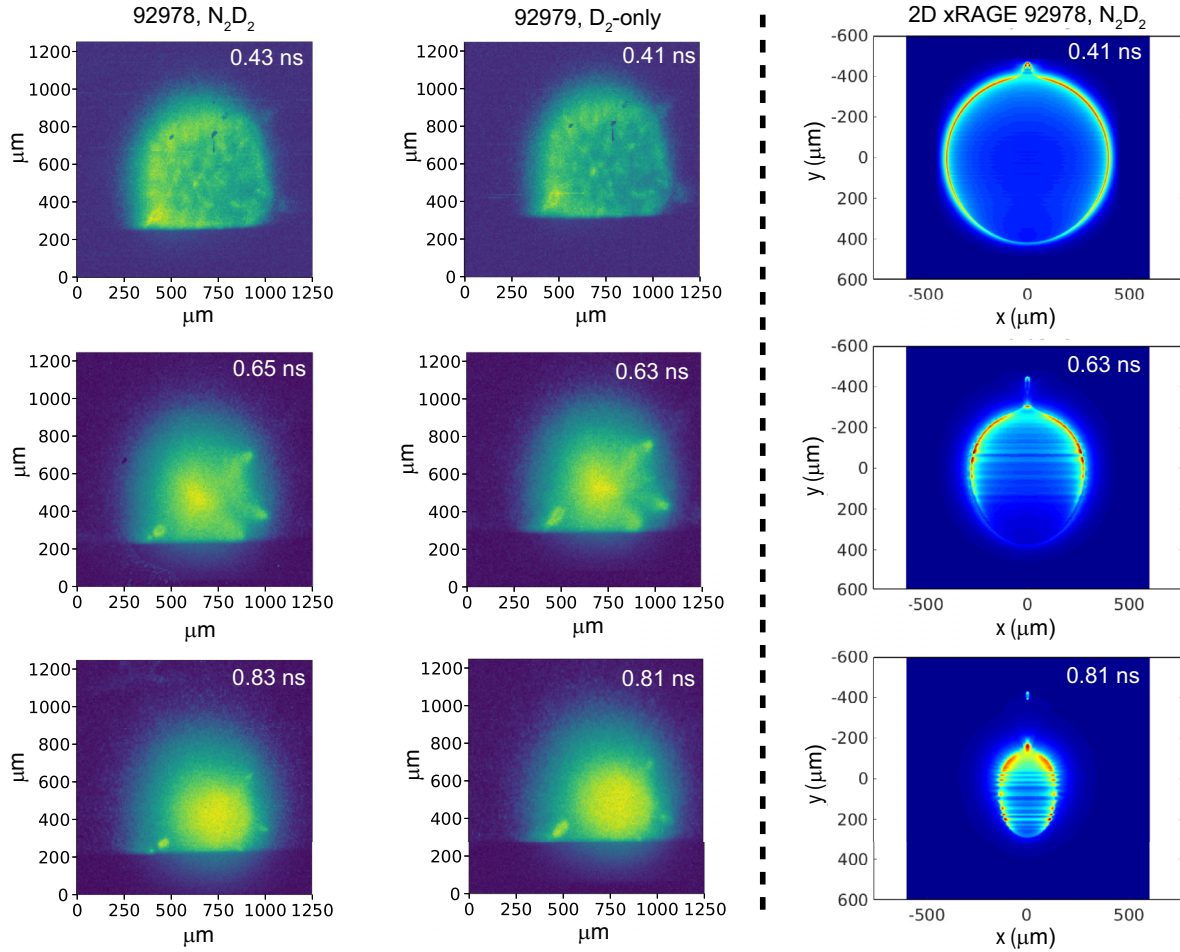


FIG. 10. Measured time-resolved x-ray images obtained with 25 μm Be filtering for observed x-ray energies > 1 keV for N_2D_2 implosion 92978 (first column) and D_2 -only implosion 92979 (second column). No obvious differences are seen between the two fill types. Also shown are synthetic xRAGE images for shot 92978 (third column) at comparable times as the measured images from the same implosion. Note that the experimental images are all clipped at the bottom due to a setup issue (the sharp cut seen in this region of the images is not a real effect), and that the 2D xRAGE simulations approximate the laser drive weak spot and capsule stalk mount to be 180° apart when experimentally they are separated by 137° .

Figure 12 shows deuterium N_k profiles versus radius at burn as calculated from the iFP with C + H simulations. Unlike from the data, the spatial scale used in the denominator in these calculations is not the estimated full extent of the fuel, but the density gradient scale length in the simulation. As can be seen, iFP estimates significant N_k for both implosion types at burn, suggesting kinetic effects are important. The numbers are also in reasonable agreement with the burn-averaged numbers estimated from observables in Sec. II. However, for the time snapshot shown in Fig. 12, N_k is substantially higher for the N_2D_2 case than for the D_2 -only case due to the lower predicted central D density, in contrast to the estimate in Sec. II.

APPENDIX C: SHOCK HEATING DYNAMICS

As alluded to in Sec. III, long-standing theory [50] suggests that viscous heating of ions in a shock front is proportional to mass as $T_{\text{ion}} \sim m_{\text{ion}} v_{\text{shock}}^2$. While the conjecture that shock

heating scales linearly with ion mass is supported by recent astrophysical [51] and ICF [52] observations, the conclusion is only expected to hold in a nonmagnetized, weakly coupled, and fully ionized plasma, and questions have been raised about the general validity of this scaling when effects other than viscosity are considered, as discussed in, e.g., Ref. [13]. The data presented here, with T_{ion} inferred from measured DD-neutron spectra observed to be higher for the N_2D_2 than for pure D_2 -fill implosions, support the conclusion that shock heating of N is stronger than shock heating of D. However, the spherically converging shock is not expected to be instantaneous in space or time, and on the timescale of heating, radiative cooling and interspecies equilibration effects play a role. Thus, while the instantaneous heating efficiency may indeed be seven times higher for N than for D, this effect cannot be immediately observed in the burn-averaged data.

The simulated time evolution of mass-weighted temperatures provides a window into the impact of spatial and temporal smearing on shock heating, and of multi-ion and

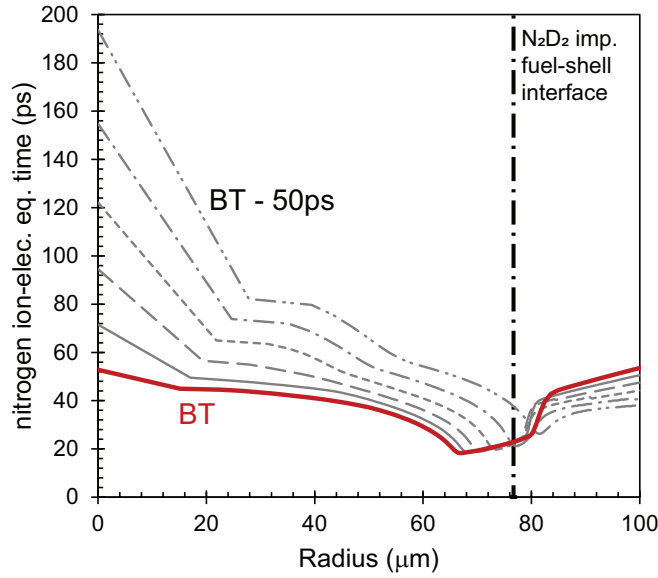


FIG. 11. HYADES-simulated nitrogen τ_{ei} at bang time (BT, red solid curve) and in steps of 10 ps prior to bang time (dashed and broken gray curves, in chronological order). The N_2D_2 fuel-shell interface at bang time is also shown (vertical black broken line).

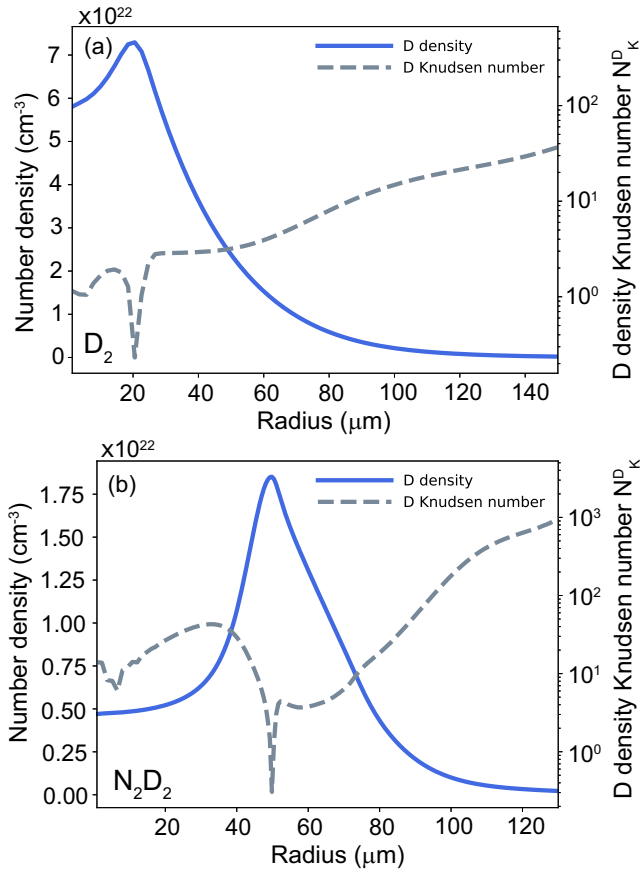


FIG. 12. iFP with C + H-simulated deuterium number density (solid blue curves) and Knudsen number (dashed gray curves) at bang time for (a) D_2 -only gas-filled and (b) N_2D_2 gas-filled implosions.

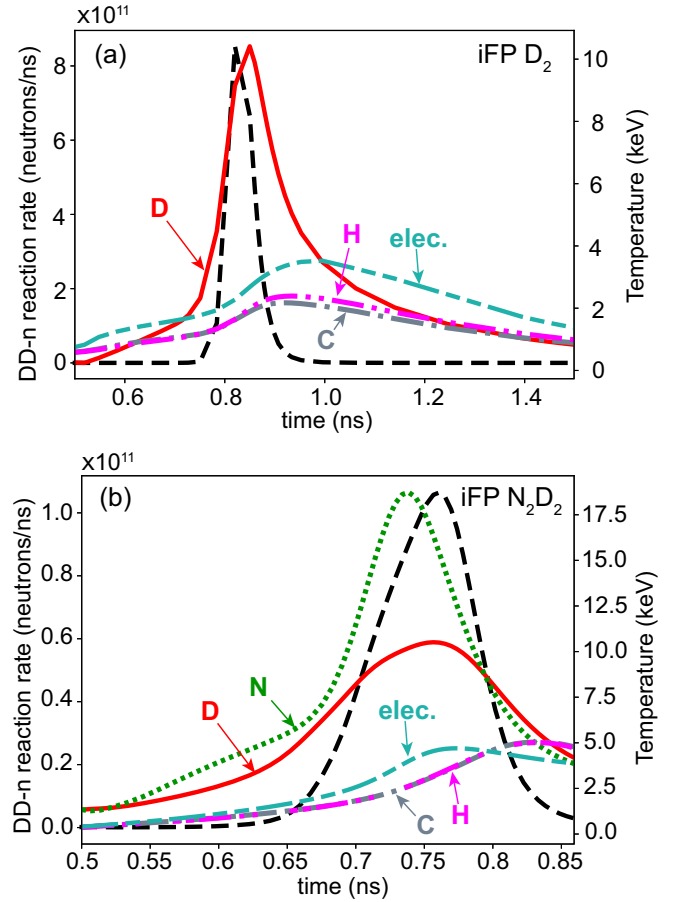


FIG. 13. Mass-weighted temperature (right-hand scale) simulated using the Vlasov-Fokker-Planck code iFP including the CH shell as two separate ion species (iFP with C+H). (a) Result for D_2 -only gas-filled implosions, and (b) results for N_2D_2 -fill implosions. The black dashed curves represent the neutron emission history (left-hand scale), and the long-short-dashed cyan curves represent the mass-averaged electron temperature. The simulations consider four ion species: D, N, C, and H. The mass-averaged $D T_{ion}$ is shown as solid red curves, the $N T_{ion}$ is shown as a dotted green curve [panel (b) only], the $C T_{ion}$ as broken gray curves, and the $H T_{ion}$ as doubly broken magenta curves.

interspecies dynamics (including equilibration) on the burn-averaged implosion output. Figure 13 shows mass-weighted T_e and T_{ion} as a function of time from the iFP with C + H simulations, with T_{ion} weighted over each particle population. Also shown are the simulated burn histories for D_2 -only and N_2D_2 implosions. Since the shock reaches different radii at different times and thus with different velocity and/or strength, this leads to a smearing relative to the traditional picture of a hydrodynamic shock front with a sudden instantaneous jump in T_{ion} (note that this effect becomes even more significant in two dimensions). As shown in Fig. 13, N reaches a mass-averaged max T_{ion} about two times that of D (not seven times). The mass-averaged T_{ion} of N and D also do not exactly track each other as they evolve in time, suggesting that the shock reaches the different ion species at different spatial and/or

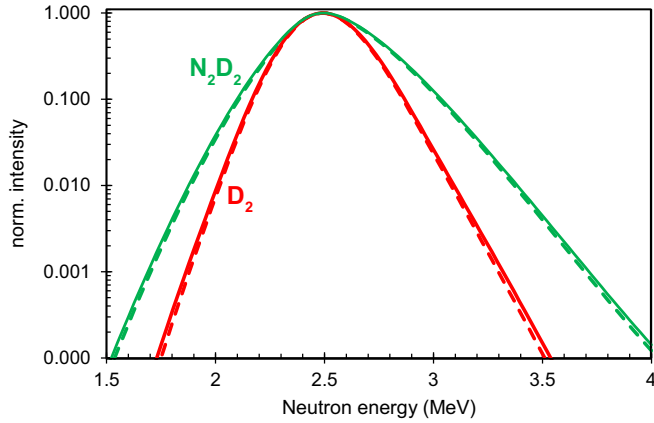


FIG. 14. Synthetic DD-neutron spectra generated by postprocessing the output from 1D HYADES simulations of the D₂-gas-filled (red, inner curves) and N₂D₂-gas-filled (green, outer curves) implosions. The dashed curves represent spectra considering thermal broadening only, while the solid curves also consider the impact of nonthermal fuel motion on the spectral broadening. Note that the solid curves represent the closest equivalent to measured data in that they do consider the flows expected to also impact the measurements. T_{ion} inferred from the width of spectra with and without considering flows are summarized in Table X.

temporal points, further complicating the picture. In fact, the iFP simulations suggest that the D-ion population is essentially free streaming; this is consistent with the burn-averaged N_k as calculated in Sec. III, which suggests very long average mean free paths for the deuterium ions in these implosions relative to system scale size. After burn, the different temperatures are also seen to converge, as a result of interspecies equilibration effects. The end result of the temporal and spatial

shock smearing, the fact that the shock reaches the different ion populations at different times, and that interspecies equilibration is constantly at play at varying rates, is that a direct comparison between N and D heating effects at the same v_{shock} cannot be made.

APPENDIX D: HYADES-SIMULATED FLOW IMPACT ON T_{ion}

Thermal and flow contributions to simulated T_{ion} can be separated in the simulations. Table X compares HYADES-simulated T_{ion} as inferred from postprocessing the simulation output in three different ways: directly burn-averaged based on temperature and density in each cell of the simulation (thus not considering flow), and inferred from synthetic neutron spectra with and without considering flow broadening, respectively. As can be seen, considering flow when generating the synthetic neutron spectrum has virtually no impact on the HYADES-inferred T_{ion} ratio, and only impacts the absolute T_{ion} difference by 0.4 keV. This result is similar to the number inferred from iFP simulations as discussed in Sec. VI, and is clearly not enough of an effect to explain the measured T_{ion} differences, thus supporting the conclusion that the mean reaction energy is indeed greater for N₂D₂ than for D₂ only.

In this analysis, T_{ion} is obtained from the synthetic neutron spectra in the same way as it is inferred from measured data, by fitting a Gaussian function to the spectrum and inferring T_{ion} from its width according to $\text{FWHM} = 82.542\sqrt{T_{\text{ion}}}$, with FWHM and T_{ion} given in keV [42]. The significant difference between HYADES burn-averaged T_{ion} and T_{ion} inferred from fitting a Gaussian to synthetic neutron spectra (Table X) arises as a result of the non-Gaussian nature of the synthetic spectra, seen in Fig. 14. Figure 14 also illustrates the subtle difference in the spectra between considering flow broadening (solid lines) and not considering flow broadening (dashed lines).

TABLE X. HYADES-simulated T_{ion} inferred in different ways. Note that while the “burn-averaged” numbers (i) are calculated directly from the simulation, the numbers inferred from the width of synthetic neutron spectra (ii, iii) are obtained by fitting a Gaussian function to the synthetic neutron spectra illustrated in Fig. 14.

Fill type	(i) Burn-averaged	(ii) Inferred from width of synthetic neutron spectrum, thermal only	(iii) Inferred from width of synthetic neutron spectrum, considering flows	Measurement (directly comparable to method iii)
N ₂ D ₂	37.30 keV	32.20 keV	33.64 keV	13.45 ± 0.39 keV
D ₂	20.87 keV	19.38 keV	20.37 keV	10.07 ± 0.34 keV
Ratio	1.79	1.66	1.65	1.34 ± 0.06

- [1] M. Gatu Johnson, A. B. Zylstra, A. Bacher, C. R. Brune, D. T. Casey, C. Forrest, H. W. Herrmann, M. Hohenberger, D. B. Sayre, R. M. Bionta, J.-L. Bourgade, J. A. Caggiano, C. Cerjan, R. S. Craxton, D. Dearborn, M. Farrell, J. A. Frenje, E. M. Garcia, V. Yu. Glebov, G. Hale, E. P. Hartouni, R. Hatarik, M. Hohensee, D. M. Holunga, M. Hoppe, R. Janezic, S. F. Khan, J. D. Kilkenny, Y. H. Kim, J. P. Knauer, T. R. Kohut, B. Lahmann, O. Landoas, C. K. Li, F. J. Marshall, L. Masse, A. McEvoy, P. McKenty, D. P. McNabb, A. Nikroo, T. G. Parham, M. Paris, R. D. Petrasso, J. Pino, P. B. Radha, B. Remington, H. G. Rinderknecht, H. Robey, M. J. Rosenberg, B. Rosse, M. Rubery, T. C. Sangster, J. Sanchez, M. Schmitt, M. Schoff, F. H. Sguin, W. Seka, H. Sio, C. Stoeckl, and B. Tipton, *Phys. Plasmas* **24**, 041407 (2017).
- [2] M. Gatu Johnson, D. T. Casey, M. Hohenberger, A. B. Zylstra, A. Bacher, C. R. Brune, R. M. Bionta, R. S. Craxton, C. L. Ellison, M. Farrell, J. A. Frenje, W. Garbett, E. M. Garcia, G. P. Grim, E. Hartouni, R. Hatarik, H. W. Herrmann, M. Hohensee, D. M. Holunga, M. Hoppe, M. Jackson, N. Kabadi, S. F. Khan, J. D. Kilkenny, T. R. Kohut, B. Lahmann, H. P. Le, C. K. Li, L. Masse, P. W. McKenty, D. P. McNabb, A. Nikroo, T. G. Parham, C. E. Parker, R. D. Petrasso, J. Pino, B. Remington, N. G. Rice, H. G. Rinderknecht, M. J. Rosenberg, J. Sanchez, D. B. Sayre, M. E. Schoff, C. M. Shuldberg, F. H. Séguin, H. Sio, Z. B. Walters, and H. D. Whitley, *Phys. Plasmas* **25**, 056303 (2018).
- [3] A. B. Zylstra, J. A. Frenje, M. Gatu Johnson, G. M. Hale, C. R. Brune, A. Bacher, D. T. Casey, C. K. Li, D. McNabb, M. Paris, R. D. Petrasso, T. C. Sangster, D. B. Sayre, and F. H. Séguin, *Phys. Rev. Lett.* **119**, 222701 (2017).
- [4] A. B. Zylstra, H. W. Herrmann, M. Gatu Johnson, Y. H. Kim, J. A. Frenje, G. Hale, C. K. Li, M. Rubery, M. Paris, A. Bacher, C. R. Brune, C. Forrest, V. Y. Glebov, R. Janezic, D. McNabb, A. Nikroo, J. Pino, T. C. Sangster, F. H. Séguin, W. Seka, H. Sio, C. Stoeckl, and R. D. Petrasso, *Phys. Rev. Lett.* **117**, 035002 (2016).
- [5] D. B. Sayre, C. R. Brune, J. A. Caggiano, V. Y. Glebov, R. Hatarik, A. D. Bacher, D. L. Bleuel, D. T. Casey, C. J. Cerjan, M. J. Eckart, R. J. Fortner, J. A. Frenje, S. Friedrich, M. Gatu-Johnson, G. P. Grim, C. Hagmann, J. P. Knauer, J. L. Kline, D. P. McNabb, J. M. McNaney, J. M. Mintz, M. J. Moran, A. Nikroo, T. Phillips, J. E. Pino, B. A. Remington, D. P. Rowley, D. H. Schneider, V. A. Smalyuk, W. Stoeffl, R. E. Tipton, S. V. Weber, and C. B. Yeamans, *Phys. Rev. Lett.* **111**, 052501 (2013).
- [6] D. T. Casey, D. B. Sayre, C. R. Brune, V. A. Smalyuk, C. R. Weber, R. E. Tipton, J. E. Pino, G. P. Grim, B. A. Remington, D. Dearborn, L. R. Benedetti, J. A. Frenje, M. Gatu-Johnson, R. Hatarik, N. Izumi, J. M. McNaney, T. Ma, G. A. Kyrala, S. MacLaren, J. Salmonson, S. F. Khan, A. Pak, L. Berzak Hopkins, S. LePape, B. K. Spears, N. B. Meezan, L. Divol, C. B. Yeamans, J. A. Caggiano, D. P. McNabb, D. M. Holunga, M. Chiarappa-Zucca, T. R. Kohut, and T. G. Parham, *Nat. Phys.* **13**, 1227 (2017).
- [7] M. Gatu Johnson, C. J. Forrest, D. B. Sayre, A. Bacher, J.-L. Bourgade, C. R. Brune, J. A. Caggiano, D. T. Casey, J. A. Frenje, V. Yu. Glebov, G. M. Hale, R. Hatarik, H. W. Herrmann, R. Janezic, Y. H. Kim, J. P. Knauer, O. Landoas, D. P. McNabb, M. W. Paris, R. D. Petrasso, J. E. Pino, S. Quaglioni, B. Rosse, J. Sanchez, T. C. Sangster, H. Sio, W. Shmayda, C. Stoeckl, I. Thompson, and A. B. Zylstra, *Phys. Rev. Lett.* **121**, 042501 (2018).
- [8] A. B. Zylstra, H. W. Herrmann, Y. H. Kim, A. McEvoy, J. A. Frenje, M. Gatu Johnson, R. D. Petrasso, V. Yu. Glebov, C. Forrest, J. Delettrez, S. Gales, and M. Rubery, *Phys. Rev. C* **101**, 042802(R) (2020).
- [9] T. R. Boehly, D. L. Brown, R. S. Craxton, R. L. Keck, J. P. Knauer, J. H. Kelly, T. J. Kessler, S. A. Kumpan, S. J. Loucks, S. A. Letzring, F. J. Marshall, R. L. McCrory, S. F. B. Morse, W. Seka, J. M. Sours, and C. P. Verdon, *Opt. Commun.* **133**, 495 (1997).
- [10] M. Gittings, R. Weaver, M. Clover, T. Betlach, N. Byrne, R. Coker, E. Dendy, R. Hueckstaedt, K. New, W. R. Oakes, D. Ranta, and R. Stefan, *Comput. Sci. Discovery* **1**, 015005 (2008).
- [11] B. M. Haines, G. P. Grim, J. R. Fincke, R. C. Shah, C. J. Forrest, K. Silverstein, F. J. Marshall, M. Boswell, M. M. Fowler, R. A. Gore, A. C. Hayes-Sterbenz, G. Jungman, A. Klein, R. S. Rundberg, M. J. Steinkamp, and J. B. Wilhelmy, *Phys. Plasmas* **23**, 072709 (2016).
- [12] B. M. Haines, C. H. Aldrich, J. M. Campbell, R. M. Rauenzahn, and C. A. Wingate, *Phys. Plasmas* **24**, 052701 (2017).
- [13] W. T. Taitano, L. Chacón, and A. N. Simakov, *J. Comput. Phys.* **297**, 357 (2015); **318**, 391 (2016); **339**, 453 (2017); **365**, 173 (2018).
- [14] B. D. Keenan, A. N. Simakov, W. T. Taitano, and L. Chacón, *Phys. Plasmas* **25**, 032103 (2018).
- [15] W. T. Taitano, A. N. Simakov, L. Chacón, and B. Keenan, *Phys. Plasmas* **25**, 056310 (2018).
- [16] S. E. Anderson, W. T. Taitano, and L. Chacon, *J. Comput. Phys.* **419**, 109686 (2020).
- [17] W. T. Taitano, B. D. Keenan, L. Chacon, S. E. Anderson, H. R. Hammer, and A. N. Simakov, *Comput. Phys. Commun.* **263**, 107861 (2021).
- [18] W. T. Taitano, L. Chacón, A. N. Simakov, and S. E. Anderson, *Comput. Phys. Commun.* **258**, 107547 (2021).
- [19] J. T. Larsen and S. M. Lane, *J. Quant. Spectrosc. Radiat. Transfer* **51**, 179 (1994).
- [20] J. R. Rygg, J. A. Frenje, C. K. Li, F. H. Séguin, R. D. Petrasso, J. A. Delettrez, V. Yu. Glebov, V. N. Goncharov, D. D. Meyerhofer, S. P. Regan, T. C. Sangster, and C. Stoeckl, *Phys. Plasmas* **13**, 052702 (2006).
- [21] D. T. Casey, J. A. Frenje, M. Gatu Johnson, M. J.-E. Manuel, H. G. Rinderknecht, N. Sinenian, F. H. Séguin, C. K. Lick, R. D. Petrasso, P. B. Radha *et al.*, *Phys. Rev. Lett.* **108**, 075002 (2012).
- [22] Y. Kim, H. W. Herrmann, N. M. Hoffman, M. J. Schmitt, G. Kagan, A. M. McEvoy, A. B. Zylstra, J. M. Smidt, S. Gales, A. Leatherland, M. Rubery, M. Gatu Johnson, J. A. Frenje, V. Yu. Glebov, and C. Forrest, *Phys. Plasmas* **28**, 012707 (2021).
- [23] H. G. Rinderknecht, M. J. Rosenberg, C. K. Li, N. M. Hoffman, G. Kagan, A. B. Zylstra, H. Sio, J. A. Frenje, M. Gatu Johnson, F. H. Séguin *et al.*, *Phys. Rev. Lett.* **114**, 025001 (2015).
- [24] P. Amendt, O. L. Landen, H. F. Robey, C. K. Li, and R. D. Petrasso, *Phys. Rev. Lett.* **105**, 115005 (2010).
- [25] P. Amendt, S. C. Wilks, C. Bellei, C. K. Li, and R. D. Petrasso, *Phys. Plasmas* **18**, 056308 (2011).
- [26] O. Larroche, *Phys. Plasmas* **19**, 122706 (2012).
- [27] C. Bellei, P. A. Amendt, S. C. Wilks, M. G. Haines, D. T. Casey, C. K. Li, R. Petrasso, and D. R. Welch, *Phys. Plasmas* **20**, 012701 (2013).

- [28] A. Inglebert, B. Canaud, and O. Larroche, *Eur. Phys. Lett.* **107**, 65003 (2014).
- [29] C. Bellei, H. Rinderknecht, A. Zylstra, M. Rosenberg, H. Sio, C. K. Li, R. Petrasso, S. C. Wilks, and P. A. Amendt, *Phys. Plasmas* **21**, 056310 (2014).
- [30] N. M. Hoffman, G. B. Zimmerman, K. Molvig, H. G. Rinderknecht, M. J. Rosenberg, B. J. Albright, A. N. Simakov, H. Sio, A. B. Zylstra, M. Gatu Johnson *et al.*, *Phys. Plasmas* **22**, 052707 (2015).
- [31] S. C. Hsu, T. R. Joshi, P. Hakel, E. L. Vold, M. J. Schmitt, N. M. Hoffman, R. M. Rauenzahn, G. Kagan, X.-Z. Tang, R. C. Mancini *et al.*, *Eur. Phys. Lett.* **115**, 65001 (2016).
- [32] T. R. Joshi, P. Hakel, S. C. Hsu, E. L. Vold, M. J. Schmitt, N. M. Hoffman, R. M. Rauenzahn, G. Kagan, X.-Z. Tang, R. C. Mancini *et al.*, *Phys. Plasmas* **24**, 056305 (2017).
- [33] T. R. Joshi, S. C. Hsu, P. Hakel, N. M. Hoffman, H. Sio, and R. C. Mancini, *Phys. Plasmas* **26**, 062702 (2019).
- [34] D. C. Wilson, G. A. Kyrala, J. F. Benage, Jr., F. J. Wysocki, M. A. Gunderson, W. J. Garbett, V. Yu. Glebov, J. Frenje, B. Yaakobi, H. W. Herrmann, J. H. Cooley, L. Welsler-Sherrill, C. J. Horsfield, and S. A. Roberts, *J. Phys: Conf. Ser.* **112**, 022015 (2008).
- [35] G. A. Kyrala, D. C. Wilson, J. F. Benage, M. Gunderson, K. Klare, J. Frenje, R. Petrasso, W. Garbett, S. James, V. Glebov, and B. Yaakobi, *High Energy Density Phys.* **3**, 163 (2007).
- [36] A. R. Miles, H.-K. Chung, R. Heeter, W. Hsing, J. A. Koch, H.-S. Park, H. F. Robey, H. A. Scott, R. Tommasini, J. Frenje, C. K. Li, R. Petrasso, V. Glebov, and R. W. Lee, *Phys. Plasmas* **19**, 072702 (2012).
- [37] B. J. Albright, T. J. Murphy, B. M. Haines, M. R. Douglas, J. H. Cooley, T. H. Day, N. A. Denissen, C. Di Stefano, P. Donovan, S. L. Edwards *et al.*, *Phys. Plasmas* **29**, 022702 (2022).
- [38] Y. Pu, X. Luo, L. Zhang, C. Sun, Z. Hu, G. Shen, X. Wang, Q. Tang, Z. Yuan, F. Wang *et al.*, *Phys. Rev. E* **102**, 023204 (2020).
- [39] J. J. MacFarlane, *J. Quant. Spectrosc. Radiat. Transfer* **81**, 287 (2003).
- [40] V. Yu. Glebov, T. C. Sangster, C. Stoeckl, J. P. Knauer, W. Theobald, K. L. Marshall, M. J. Shoup III, T. Buczek, M. Cruz, T. Duffy, M. Romanofsky, M. Fox, A. Pruyne, M. J. Moran, R. A. Lerche, J. McNaney, J. D. Kilkenny, M. J. Eckart, D. Schneider, D. Munro, W. Stoeffl, R. Zacharias, J. J. Haslam, T. Clancy, M. Yeoman, D. Warwas, C. J. Horsfield, J.-L. Bourgade, O. Landoas, L. Disdier, G. A. Chandler, and R. J. Leeper, *Rev. Sci. Instrum.* **81**, 10D325 (2010); University of Rochester, Laboratory for Laser Energetics, National Laser Users' Facility Users Guide, http://www.lle.rochester.edu/media/about/documents/UsersGuide/05_UsersGuide.pdf (2014).
- [41] C. J. Forrest, V. Yu. Glebov, V. N. Goncharov, J. P. Knauer, P. B. Radha, S. P. Regan, M. H. Romanofsky, T. C. Sangster, M. J. Shoup III, and C. Stoeckl, *Rev. Sci. Instrum.* **87**, 11D814 (2016).
- [42] L. Ballabio, J. Källne, and G. Gorini, *Nucl. Fusion* **38**, 1723 (1998).
- [43] B. Appelbe and J. Chittenden, *Plasma Phys. Control. Fusion* **53**, 045002 (2011).
- [44] T. J. Murphy, *Phys. Plasmas* **21**, 072701 (2014).
- [45] B. K. Spears, M. J. Edwards, S. Hatchett, J. Kilkenny, J. Knauer, A. Kritcher, J. Lindl, D. Munro, P. Patel, H. F. Robey, and R. P. J. Town, *Phys. Plasmas* **21**, 042702 (2014).
- [46] M. Gatu Johnson, J. P. Knauer, C. J. Cerjan, M. J. Eckart, G. P. Grim, E. P. Hartouni, R. Hatarik, J. D. Kilkenny, D. H. Munro, D. B. Sayre, B. K. Spears, R. M. Bionta, E. J. Bond, J. A. Caggiano, D. Callahan, D. T. Casey, T. Döppner, J. A. Frenje, V. Yu. Glebov, O. Hurricane, A. Kritcher, S. LePape, T. Ma, A. Mackinnon, N. Meezan, P. Patel, R. D. Petrasso, J. E. Ralph, P. T. Springer, and C. B. Yeamans, *Phys. Rev. E* **94**, 021202(R) (2016).
- [47] D. H. Munro, *Nucl. Fusion* **56**, 036001 (2016).
- [48] M. Gatu Johnson, B. D. Appelbe, J. P. Chittenden, J. Delettrez, C. Forrest, J. A. Frenje, V. Yu. Glebov, W. Grimble, B. M. Haines, I. Igumenshchev, R. Janezic, J. P. Knauer, B. Lahmann, F. J. Marshall, T. Michel, F. H. Séguin, C. Stoeckl, C. Walsh, A. B. Zylstra, and R. D. Petrasso, *Phys. Rev. E* **98**, 051201(R) (2018).
- [49] C. Stoeckl, R. Boni, F. Ehrne, C. J. Forrest, V. Yu. Glebov, J. Katz, D. J. Lonobile, J. Magoon, S. P. Regan, M. J. Shoup III, A. Sorce, C. Sorce, T. C. Sangster, and D. Weiner, *Rev. Sci. Instrum.* **87**, 053501 (2016).
- [50] Y. B. Zel'dovich and Y. P. Raizer, *Physics of Shock Waves and High-Temperature Hydrodynamic Phenomena*, edited by W. D. Hayes, and R. F. Probstein (Academic Press, New York, 1967), Vol. 2, pp. 515–520.
- [51] M. Miceli, S. Orlando, D. N. Burrows, K. A. Frank, C. A. Argiroffi, F. Reale, G. Peres, O. Petruk, and F. Bocchino, *Nat. Astron.* **3**, 236 (2019).
- [52] N. V. Kabadi, R. Simpson, P. J. Adrian, A. Bose, J. A. Frenje, M. Gatu Johnson, B. Lahmann, C. K. Li, C. E. Parker, F. H. Séguin *et al.*, *Phys. Rev. E* **104**, L013201 (2021).
- [53] P. J. Adrian, J. Frenje, B. Aguirre, B. Bachmann, A. Birkel, M. Gatu Johnson, N. V. Kabadi, B. Lahmann, C. K. Li, O. M. Mannion, W. Martin, Z. L. Mohamed, S. P. Regan, H. G. Rinderknecht, B. Scheiner, M. J. Schmitt, F. H. Séguin, R. C. Shah, H. Sio, C. Sorce, G. D. Sutcliffe, and R. D. Petrasso, *Rev. Sci. Instrum.* **92**, 043548 (2021).
- [54] K. Molvig, N. M. Hoffman, B. J. Albright, E. M. Nelson, and R. B. Webster, *Phys. Rev. Lett.* **109**, 095001 (2012).
- [55] B. J. Albright, K. Molvig, C.-K. Huang, A. N. Simakov, E. S. Dodd, N. M. Hoffman, G. Kagan, and P. F. Schmit, *Phys. Plasmas* **20**, 122705 (2013).
- [56] E. L. Vold, R. M. Rauenzahn, C. H. Aldrich, K. Molvig, A. N. Simakov, and B. M. Haines, *Phys. Plasmas* **24**, 042702 (2017).
- [57] J. A. Marozas, M. Hohenberger, M. J. Rosenberg, D. Turnbull, T. J. B. Collins, P. B. Radha, P. W. McKenty, J. D. Zuegel, F. J. Marshall, S. P. Regan, T. C. Sangster, W. Seka, E. M. Campbell, V. N. Goncharov, M. W. Bowers, J.-M. G. Di Nicola, G. Erbert, B. J. MacGowan, L. J. Pelz, J. Moody, and S. T. Yang, *Phys. Plasmas* **25**, 056314 (2018).
- [58] H.-S. Bosch and G. M. Hale, *Nucl. Fusion* **32**, 611 (1992).
- [59] H. G. Rinderknecht, H. Sio, C. K. Li, A. B. Zylstra, M. J. Rosenberg, P. Amendt, J. Delettrez, C. Bellei, J. A. Frenje, M. Gatu Johnson, F. H. Séguin, R. D. Petrasso, R. Betti, V. Yu. Glebov, D. D. Meyerhofer, T. C. Sangster, C. Stoeckl, O. Landen, V. A. Smalyuk, S. Wilks, A. Greenwood, and A. Nikroo, *Phys. Rev. Lett.* **112**, 135001 (2014).
- [60] A. B. Zylstra, N. M. Hoffman, H. W. Herrmann, M. J. Schmitt, Y. H. Kim, K. Meaney, A. Leatherland, S. Gales, C. Forrest, V. Yu. Glebov, M. Schoff, M. Hoppe, and N. Ravelo, *Phys. Rev. E* **97**, 061201(R) (2018).

- [61] H. Sio, O. Larroche, A. Bose, S. Atzeni, J. A. Frenje, N. V. Kabadi, M. Gatu Johnson, C. K. Li, V. Glebov, C. Stoeckl, B. Lahmann, P. J. Adrian, S. P. Regan, A. Birkel, F. H. Seguin, and R. D. Petrasso, *Phys. Plasmas* **29**, 072710 (2022).
- [62] H. Sio, J. A. Frenje, A. Le, S. Atzeni, T. J. T. Kwan, M. Gatu Johnson, G. Kagan, C. Stoeckl, C. K. Li, C. E. Parker *et al.*, *Phys. Rev. Lett.* **122**, 035001 (2019).
- [63] A. L. Velikovich, K. G. Whitney, and J. W. Thornhill, *Phys. Plasmas* **8**, 4524 (2001).
- [64] M. Gatu Johnson, B. M. Haines, C. Forrest, J. A. Frenje, V. Yu. Glebov, W. Grimble, R. Janezic, J. P. Knauer, B. Lahmann, F. J. Marshall, T. Michel, F. H. Séguin, C. Stoeckl, and R. D. Petrasso, *High Energy Density Phys.* **36**, 100825 (2020).
- [65] M. Gatu Johnson, P. J. Adrian, K. S. Anderson, B. D. Appelbe, J. P. Chittenden, A. J. Crilly, D. Edgell, C. J. Forrest, J. A. Frenje, V. Yu. Glebov, B. M. Haines, I. Igumenshchev, D. Jacobs-Perkins, R. Janezic, N. V. Kabadi, J. P. Knauer, B. Lahmann, O. M. Mannion, F. J. Marshall, T. Michel, F. H. Séguin, R. Shah, C. Stoeckl, C. A. Walsh, and R. D. Petrasso, *Phys. Plasmas* **27**, 032704 (2020).
- [66] M. Gatu Johnson, D. T. Casey, J. A. Frenje, C.-K. Li, F. H. Séguin, R. D. Petrasso, R. Ashabranner, R. Bionta, S. LePape, M. McKernan, A. Mackinnon, J. D. Kilkenny, J. Knauer, and T. C. Sangster, *Phys. Plasmas* **20**, 042707 (2013).
- [67] O. M. Mannion, V. Yu. Glebov, C. J. Forrest, J. P. Knauer, V. N. Goncharov, S. P. Regan, T. C. Sangster, C. Stoeckl, and M. Gatu Johnson, *Rev. Sci. Instrum.* **89**, 10I131 (2018).
- [68] G. Kagan, D. Svyatskiy, H. G. Rinderknecht, M. J. Rosenberg, A. B. Zylstra, C.-K. Huang, and C. J. McDevitt, *Phys. Rev. Lett.* **115**, 105002 (2015).
- [69] B. D. Appelbe, W. T. Taitano, A. J. Crilly, O. M. Mannion, C. J. Forrest, and J. P. Chittenden, *arXiv:2305.02403* (2023).
- [70] I. Garin Fernandez, Nuclear Astrophysics Experiments in Inertial Confinement Fusion Platforms: Analysis of Neutron Densities for S-process Experiments and Approximations Used in Light Ion Cross-sectional Measurements, Imperial College London Department of Physics Reports, Plas-Chittenden-1, CID 01339437 (2021).
- [71] A. Crilly, I. Garin-Fernandez, B. D. Appelbe, and J. P. Chittenden, *Front. Phys.* **10**, 937972 (2022).
- [72] D. T. Michel, A. K. Davis, W. Armstrong, R. Bahr, R. Epstein, V. N. Goncharov, M. Hohenberger, I. V. Igumenshchev, R. Jungquist, D. D. Meyerhofer, P. B. Radha, T. C. Sangster, C. Sorce, and D. H. Froula, *High Power Laser Sci. Eng.* **3**, e19 (2015).